Available online at www.sciencedirect.com

ScienceDirect

Geochimica et Cosmochimica Acta 259 (2019) 17–36

Geochimica et Cosmochimica Acta

www.elsevier.com/locate/gca

Discrepancy between bulk-rock and zircon Hf isotopes accompanying Nd-Hf isotope decoupling

Hui Huang [a,b,*], Yaoling Niu [a,c], Fang-Zhen Teng [b], Shui-Jiong Wang [a]

[a] State Key Laboratory of Geological Processes and Mineral Resources, and Institute of Earth Sciences, China University of Geosciences, Beijing 100083, China

[b] Department of Earth and Space Sciences, University of Washington, Seattle, WA 98195, USA

[c] Department of Earth Sciences, Durham University, Durham DH1 3LE, UK

Received 5 June 2018; accepted in revised form 24 May 2019; Available online 11 June 2019

Abstract

Zircon is an important accessory mineral for studying the crust-mantle interaction and crustal growth through time because zircon crystals not only allow precise dating but also record initial Hf isotope ratios of the host magma. Our study on a suite of gabbronorite, mafic diorite cumulate, diorite and granite from the Kekeli Batholith in the North Qilian Orogenic Belt, Northern Tibetan Plateau, shows (1) a significant Hf isotope discrepancy between zircon and their bulk rocks; and (2) bulk-rock Nd-Hf isotope decoupling. These observations thus demonstrate that zircons do not always capture the full history of magmatic system. The significant positive correlation between bulk-rock Hf isotope ratios and TiO_2 content ($R^2 = 0.94$) indicates that Ti-rich minerals (e.g., ilmenite, amphibole) are likely important Hf hosts. The early-formed Ti-rich minerals possibly record different Hf isotopes from those of zircons crystallized subsequently, thus causing discrepancy between zircon and bulk-rocks and leading to bulk-rock Nd-Hf isotope decoupling. Correlations between bulk-rock TiO_2 content, Mg isotopes and Hf isotopes indicate a mixing process, with granite and gabbronorite representing two compositional endmembers. Because Ti minerals have higher crystallization temperatures than zircons, when the mixing melts have contrasting isotopes (or from heterogeneous sources/have a strong crustal contamination), the bulk-rock and zircon Hf isotope discrepancies reflect mineral crystallization sequence during mafic and felsic magma mixing. It is thus imperative to consider early formed minerals such as Ti-rich minerals and the bulk rock composition, not just zircons, when using Hf isotopes to track melt evolution and precisely constrain mantle contribution to granitoid petrogenesis.

Keywords: Hf isotope discrepancy between zircons and their bulk-rocks; Nd-Hf isotope decoupling; Ti-rich mineral; North Qilian; granitoids

1. INTRODUCTION

Quantitative understanding of petrogenesis and crust-mantle evolution has advanced greatly in recent years because of increased routine analysis of zircon *in-situ* Hf isotopes. Zircon grains in common crustal rocks host a large amount of Hf in the rock and zircon Hf isotopes can thus be used to constrain the initial Hf isotopes of the bulk magma at the time of crystallization due to the very low Lu/Hf ratios in zircons (Patchett, 1983; Vervoort and Blichert-Toft, 1999; Schmitz et al., 2004; Li et al., 2010; Chu et al., 2011). Because of its advantage to unfold the timing and magnitude of different endmember input, and because of the advances in the LA-MC-ICP-MS technique, zircon (vs. bulk rock) Hf isotope composition becomes much easier to acquire, *in situ* Hf isotopic composition of zircons, rather than bulk rock samples, has thus

* Corresponding author.
E-mail address: huihuang@cugb.edu.cn (H. Huang).

https://doi.org/10.1016/j.gca.2019.05.031
0016-7037/

been widely used to reveal the petrogenesis of igneous rock in the same way as the bulk rock Nd isotopes.

However, increasing studies have shown that zircon Hf isotopes do not necessarily reflect the isotope composition of their source. Given the very low Lu/Hf ratios in zircons, zircon Hf isotopes are less radiogenic over time than non zircon phases. Disequilibrium melting of zircons would produce apparent variations of Hf isotopes in the melt (Gerdes, 2012; Tang et al., 2014; Wang et al., 2017). In mafic magmatic systems, zircons appear on the liquidus at a late stage (basaltic-andesite stage) and their Hf isotope compositions are, therefore, controlled by open-system magma chamber processes (crustal assimilation/contamination) as well as parental magmas (Dickinson and Hess, 1982; Hanchar and Watson, 2003; Zheng et al., 2006; Boehnke et al., 2013). This has been observed in post-collisional mafic magmas with zircons biasing towards crustal signatures (Couzinie et al., 2016). On the other hand, Ti minerals can host a significant portion of Zr in rocks, and are also major hosts of Hf due to the nearly identical Zr-Hf geochemical behavior. For example, ilmenite in highly fractionated intrusions contains 200–1400 ppm of Zr (Jang and Naslund, 2003) and in mafic dykes contains up to 3850 ppm of Zr (Pearce, 1990) while the Zr/Hf ratio in ilmenite generally remains chondritic (37–40, Jang and Naslund, 2003; Bea et al., 2006). Amphibole also contains significant amounts of Zr and Hf (Bea et al., 2006). It is possible that Ti-rich minerals and zircons have different Hf isotope compositions if they derive from different batches of magma or crystallize at different stages in an evolving open-system chamber. All these observations require caution in using zircon Hf isotopes to discuss sources and processes of magmatism.

Hafnium isotopes have often been used together with Nd isotopes to discuss the petrogenesis of magmatic rocks. Neodymium isotopes generally behave similarly to Hf isotopes in terrestrial rocks ($\varepsilon_{Hf} \approx 1.5 * \varepsilon_{Nd}$, Vervoort and Blichert-Toft, 1999; Chauvel et al., 2008), and thus a correlated Nd-Hf isotope variation would probably reflect relatively simple processes dominated by magmatism controlled by the relatively less incompatible behavior of the radioactive parents (Sm, Lu) over the radiogenic daughters (Nd, Hf), i.e., Kd (Sm/Nd) > 1 and Kd (Lu/Hf) > 1. Studies have discovered Nd-Hf isotope decoupling in continental lithospheric mantle rocks (Salters and Zindler, 1995; Griffin et al., 2000; Pearson and Nowell, 2003; Nowell et al., 2004), mantle-derived basalts (Chen et al., 2009; Hoffmann et al., 2010; Rizo et al., 2011; Zeng et al., 2011) and lower crustal granulites (Schmitz et al., 2004), reflecting important yet poorly understood processes. By contrast, Nd-Hf isotope relationship in granitoids is relatively less discussed, largely because that the large variation of zircon *in situ* ε_{Hf} values is common. Huang et al. (2017) discussed a special case for granites from the Qilian Jinfosi Batholith with decoupled bulk rock Nd-Hf isotopes interpreted as being produced by reworking of ancient garnet-bearing residue. If Hf isotopes in zircons and bulk rocks do not always equal, it is important to understand the origins of Hf isotope discrepancies between them before using Nd-Hf isotopes to discuss the petrogenesis of the granitoids under study.

In this paper, we report bulk-rock major and trace element compositions, zircon geochoronology, zircon Hf isotopes and Sr-Nd-Pb-Hf-Mg isotope geochemistry for a granitoid sample suite in the Qilian Orogenic Belt, on the northern Tibetan Plateau. Our results suggest that the likely scenario responsive for Nd-Hf isotope decoupling is that Ti-rich minerals can buffer Hf isotopes of bulk rocks. Previous studies suggest that Ti-rich cumulates have heavier Mg isotopic compositions than normal igneous rocks (Wang et al., 2014), probably because Ti-rich minerals, such as ilmenite, have extremely heavier Mg isotope compositions than silicate minerals (Chen et al., 2018). Thus, Mg isotopes are also applied to better understand the petrogenesis of the sample suite. The significant discrepancy between zircon and bulk-rock Hf isotopes, and the decoupling between bulk-rock Nd and Hf isotopes indicate that zircons do not always trustfully capture the full magmatic history of igneous rocks that evolved in an open system involving interactions between isotopically contrasting magmas, in which case, Hf isotopes of early formed minerals (e.g., Ti-rich minerals) and/or bulk rocks are needed when discussing the petrogenesis of granitoids.

2. GEOLOGICAL BACKGROUND

The North Qilian Orogenic Belt (NQOB) is regarded as a typical oceanic suture zone on the northernmost margin of the Greater Tibetan Plateau (Fig. 1). It contains ophiolite sequences, metamorphic rock assemblages and magmatic rocks. The magmatic rocks are largely arc related volcanic rocks and I-type granitoid plutons dated from 516 Ma to 446 Ma (Wang et al., 2005; Chen et al., 2014). The subduction-related high pressure (HP) metamorphic rocks structurally coexist with magmatic rocks (Wu et al., 1993; Zhang et al., 1997, 2007; Liu et al., 2006; Song et al., 2004, 2006). HP rocks in the NQOB include low-grade blueschist rocks and high-grade blueschist assemblages (Song et al., 2013). Metamorphic P-T conditions for the low-grade blueschist rocks are 250—375 °C and 0.6–1.1 GPa (Song et al., 2009; Zhang et al., 2009). P-T conditions for the high-grade blueschist rocks are 445–530 °C and 2.15–2.5 GPa (Song et al., 2007; Yu et al., 2009). Metamorphic ages for the high-grade blueschists range from 463 Ma to 489 Ma whereas the low-grade blueschists are much younger (Lin et al., 2010).

From south to north, the NQOB is subdivided into southern ophiolite belt, middle arc magmatic belt and northern back-arc ophiolite-volcanic belt (Fig. 1) (Song et al., 2013). Mantle peridotites, mafic-ultramafic cumulates and basalts are found within the southern ophiolite belt, indicating seafloor spreading at ~560–500 Ma (Shi et al., 2004; Tseng et al., 2007; Song et al., 2009, 2013). The middle arc magmatic belt consists of boninite, arc-volcanic complex and granitoids. The boninite complex was produced from continuous melting of a mantle wedge during ~517–487 Ma (Xia et al., 2012). The arc-volcanic complex consists of mostly felsic rocks with a small amount of intermediate to mafic rocks of ~500–450 Ma (Wang et al., 2005; Song et al., 2013). The northern back-arc sub-belt consists of ~490–449 Ma ultramafic rocks, cumulates and basalts,

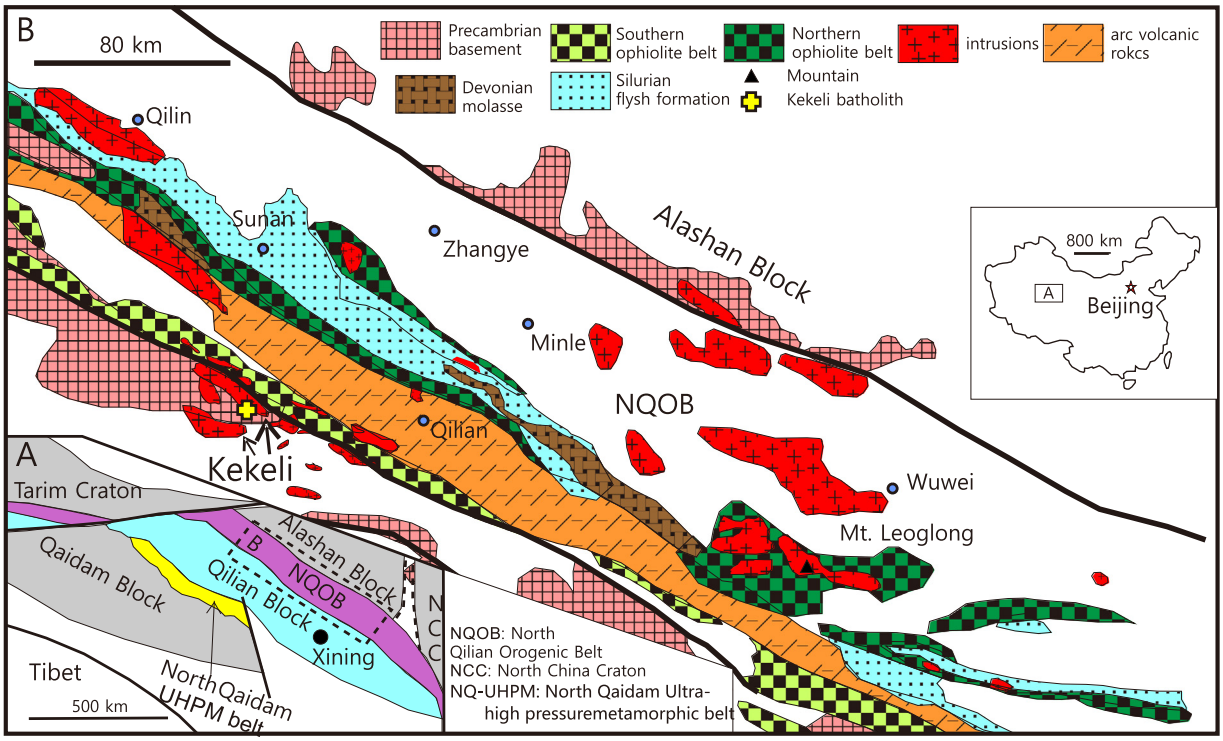

Fig. 1. Schematic map showing major tectonic units of West China and the North Qilian Orogenic Belt after Song et al., (2013) and Huang et al., (2017).

indicating a back-arc extension setting (Song et al., 2009, 2013; Xia and Song, 2010; Xia et al., 2012).

The Kekeli batholith is located within the southern ophiolite belt of the North Qilian Orogenic Belt, intruding the Precambrian meta-volcanic, pelitic and clastic rocks. This batholith is mostly diorite-granodiorite with minor plagiogranite (Wu et al., 2010), and is characterised by the presence of a large amount of mafic magmatic enclaves (MMEs) (Fig. 2). The contacts between MMEs and host rocks are gradational and some of them show interaction with the host rock. Wu et al. (2010) report an age of 501 Ma for the granodiorite and an age of 512 Ma for the plagiogranite from the Kekeli Batholith. They suggest that the granodiorite was derived from subducted oceanic crust while the plagiogranite was produced by partial melting of gabbro based on the age constraint and petrologic observations.

3. PETROLOGY

Samples from the Kekeli batholith include gabbronorite, mafic diorite cumulate, host diorite and granite, of which gabbronorite and cumulates occur as enclaves in the host diorite (Fig. 2). Sample details and mineral assemblages are given in Table 1. Mineral assemblages were obtained by point counting. The textures under microscope show that samples are not affected by metamorphism except one sample with greenschist mineral overprint (see below).

The granite has a mineral assemblage of plagioclase (Pl), K-feldspar (Kfs), quartz (Qtz) and biotite (Bt) (Fig. 2) with accessory minerals of apatite and zircon. The granite has no enclaves. The diorite contains a large number of mafic enclaves (Fig. 2). The enclaves are fine-grained and darker than the host. They are rounded or ovoid, but some are irregular, commonly 10–50 cm in diameter. Their contacts with the host can be sharp, gradational or in jigsaw shape (Fig. 2). The enclaves include two types of MMEs: mafic diorite and gabbronorite. The mafic diorite has cumulative and heteradcumulate textures and contains dominantly amphibole and plagioclase as well as various quartz and K-feldspar as interstitial phases (Fig. 2). Overprint of greenschist facies metamorphism is apparent in one sample (QL10-27; tremolite, actinolite, epidote, chlorite, etc.). The cumulate textures in the mafic diorite and the same mineralogy as in their host indicate that the mafic diorite is the cumulate crystallized from their host magma (Niu et al., 2013; Huang et al., 2014; Chen et al., 2016). The gabbronorite also appears as an enclave in the host and much rare than the mafic diorite. It is ~20 cm in diameter and has a gradational contact with the host showing increasing modal pyroxene. This transitional rind is about 2–3 cm wide. The gabbronorite has a mineral assemblage of orthopyroxene (Opx), clinopyroxene (Cpx), plagioclase (Pl), ilmenite (ilm) (~4% modal abundances) and accessory minerals (Table 1, Fig. 2). Pyroxene (Px, include Cpx and Opx) is characterized by replacement rims of amphibole (Amp) and biotite (Bt) (Fig. 2). Accessory minerals such as apatite and zircon are also present. The gabbronorite has different minerals from the host diorite and shows no cumulative texture, indicating its non-cumulative origin.

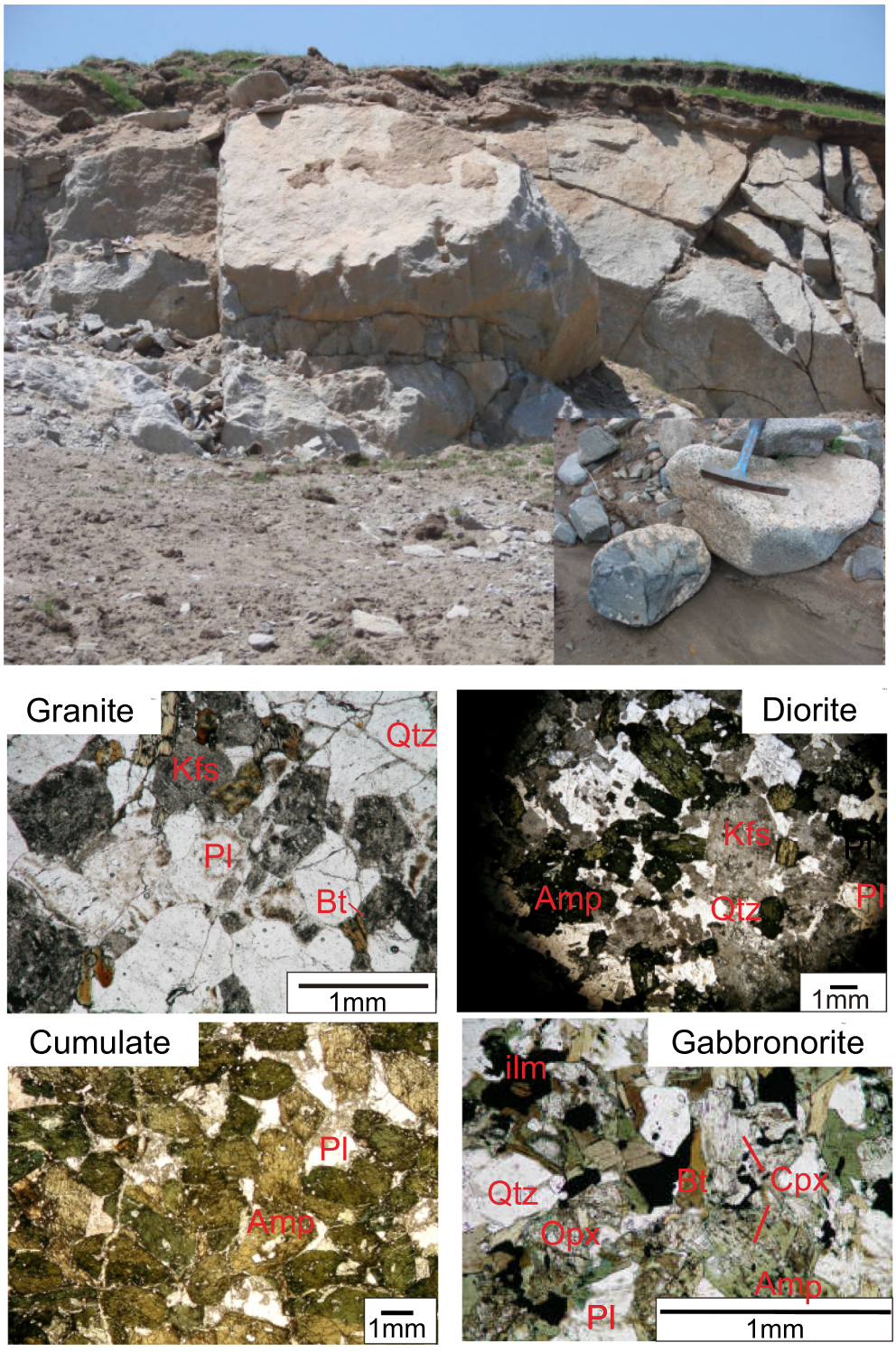

Fig. 2. Field photos of the Kekeli Batholith and photomicrographs under plane polarized light of the representative granite, diorite, cumulate and gabbronorite.

4. METHODS

Each sample was cut into 3 splits for thin section, bulk-rock powder and zircon selection, respectively. For geochemical analysis, all the rock chips were fresh with weathered surfaces and pen/saw marks removed and then cleaned in 5% HCl and Milli-Q H_2O ultrasonic bath before powdering in agate mills in an clean environment

Table 1
Sample location and brief description of samples Kekeli, the North Qtzilian Orogenic Belt.

Sample	Age (Ma)	GPS position		Mineral assemblage
QL10-14	501	N38°24′45.7′′	E99°25′38.1′′	Granite, Bt13%, Pl30%, Kfs15%, Qtz42%
QL10-15	501	N38°24′45.7′′	E99°25′38.1′′	Granite, Bt/Chl22%, Kfs11%, Pl20%, Qtz46%
QL10-20		N38°23′49.3′′	E99°20′07.7′′	Cumulate, Amp50%, Pl26%, Kfs10%, Qtz10%, Ep2.5%, ilm1.6%
QL10-21	503	N38°23′49.3′′	E99°20′07.7′′	Cumulate, Amp62%, Pl23%, Kfs, Qtz13%, Ep0.75%
QL10-22		N38°23′49.3′′	E99°20′07.7′′	Cumulate, Amp80%, interstitial Pl, Kf, Qtz, cumulate texture
QL10-23	502	N38°23′49.3′′	E99°20′07.7′′	Diorite, Amp27%, Pl44%, Kfs10%, Qtz16%
QL10-24	500	N38°23′49.3′′	E99°20′07.7′′	Diorite, Amp24%, Pl36%, Kfs25%, Qtz15%
QL10-25	500	N38°23′49.3′′	E99°20′07.7′′	Cumulate, Tremolite (Amp) 64%, Pl34%,Kfs0.5%.Qtz 1.75%
QL10-26	500	N38°23′49.3′′	E99°20′07.7′′	Gabbronorite, Pyroxene28%, Bt10%, Amp12%, Qtz18%, Pl18%, Kfs:9%, Fe-Ti oxides: 4.2%
QL10-27	500	N38°23′49.3′′	E99°20′07.7′′	Diorite, tremolite34%,Pl 25%, Qtz 30%, Kfs10%

(see Huang et al., 2014). Zircons were extracted using heavy liquid and magnetic separation methods.

4.1. Bulk rock major and trace elements

Bulk-rock major element analysis was done using X-ray fluorescence (XRF) on fused glass disks in the Tianjin Institute of Geology and Mineral Resources, China following the method of Li et al. (2011). Trace element analysis was done using acid digestion in bombs and inductively coupled plasma mass spectrometer (ICP-MS, Thermo Scientific X seriesII) in the Tianjin Institute of Geology and Mineral Resources. The precision on standards (GSR-1, GSR-3, GSR-8, GSR-9) was better than 3% and mostly better than 0.5%. Zircons were selected and mounted under a binocular microscope. Cathodoluminescence (CL) images were taken to document the internal structures of zircon crystals. All the zircon grains are ~100–300 μm.

4.2. Bulk rock Sr-Nd-Pb-Hf isotope analysis

The bulk-rock Sr-Nd-Pb-Hf isotopes were measured using Neptune multicollector inductively coupled plasma spectrometry (MC-ICP-MS) at the Arthur Holmes Isotope Geology Laboratory at Durham University, UK. About 100 mg of sample powder was dissolved in distilled 29 M HF and 16 M HNO_3 mixtures in screw-top Savillex Teflon beakers on a hotplate for 1–5 days and occasionally put into ultrasonic bath to promote complete dissolution. Sr, Pb and Nd-Hf fractions were separated using Sr-spec resin columns to obtain pure Sr, Pb fractions and Nd-Hf bearing fractions. The Nd-Hf fraction was then separated by Hf-Nd cation exchange resin (Bio-Rad AG50X-8) column following the Hf-Ti anion exchange columns to remove any Ti that may have remained in Hf fraction. The international rock standard BHVO-1 and blank samples were processed simultaneously with samples from weighing till final analysis per sample batch during the analytical session.

All the isotope fractions from ion-exchange columns were evaporated to white paste dryness, dissolved in 6N HCl, heated to dryness and then Sr, Nd, and Pb fractions were taken up in 1 mL 3% HNO_3 solution and Hf fractions were taken up in 0.5 ml 3% HNO_3–1NHF. Sr, Nd, and Pb samples were introduced into instrument using an ESI PFA-50 microflow nebuliser and a dual cyclonic-Scott Double Pass spraychamber. With this sample introduction set up, the H skimmer cone was used. Hf fractions were introduced into an ESI PFA50 nebulizer together with a Cetac Aridus desolvator. With this sample introduction set up, the high sensitivity X skimmer cone was used and the sensitivity for Hf on the Neptune was 400 V/total Hf ppm. For each element, the analysis was based on the average of 50 measurement cycles with an integration time of 4 seconds per cycle. Sample uptake rates were 100 μl/min. Details of instrument operating conditions are presented in Nowell et al. (2003) and Dowall et al. (2003). The long-term performance of the Durham Neptune for the Sr-Nd-Hf isotopes is given in Nowell et al. (2003). The international standards NBS987, J&M, NBS981 and JMC475 were analysed every five samples to monitor the instrument drift and data quality for Sr, Nd, Pb and Hf isotope analyses, respectively.

The Sr standard NBS987 yielded average $^{87}Sr/^{86}Sr$ of 0.710277 ± 0.000020 (2SD, $n = 39$). All the data were normalized to the accepted $^{87}Sr/^{86}Sr$ ratio for NBS 987 of 0.71024 (Thirlwall, 1991). Total analytical blanks for Sr isotopes were <100 pg. The average $^{143}Nd/^{144}Nd$ for both pure and Sm-doped J&M was 0.511107 ± 0.00012 (2SD, $n = 47$) with all data normalized to the accepted $^{143}Nd/^{144}Nd$ ratio for J&M of 0.511110 (Thirlwall, 1991). The $^{143}Nd/^{144}Nd$ ratio for international rock BHVO-1 was 0.512988 ± 0.000008 (2SD, $n = 5$) which is in agreement with 0.512986 ± 0.000009 by Weis et al. (2005). Total analytical blanks for Nd isotopes were below 37 pg. For Pb isotopes, mass bias was corrected for using $^{205}Tl/^{203}Tl$ ratios and an exponential law. The best fit ratio for all the Pb ratios was determined for each analytical session by minimizing the difference in offset between all the Pb ratios and the Galer (1999) values. $^{205}Tl/^{203}Tl$ ratio in this analytical session for mass bias was 2.38854. The average ratios for NBS981 were $^{206}Pb/^{204}Pb = 16.941 \pm 0.001$, $^{207}Pb/^{204}Pb = 15.497 \pm 0.001$, $^{208}Pb/^{204}Pb = 36.716 \pm 0.002$. The $^{206}Pb/^{204}Pb$, $^{207}Pb/^{204}Pb$ and $^{208}Pb/^{204}Pb$ ratios for BHVO-1 were 18.689, 15.576 and 38.366, in agreement with the GEOREM accepted value ($^{206}Pb/^{204}Pb = 18.692 \pm 0.008$, $^{207}Pb/^{204}Pb = 15.572 \pm 0.006$, $^{208}Pb/^{204}Pb = 38.355 \pm 0.022$). Total blanks for Pb isotopes were below 90 pg.

For Hf isotopes, instrumental mass bias was corrected using a $^{179}Hf/^{177}Hf$ ratio of 0.7325 and an exponential law. Corrections for isobaric interferences from ^{176}Yb and ^{175}Lu on ^{176}Hf were made by monitoring $^{172\text{-}173}Yb$ and ^{175}Lu. The average $^{176}Hf/^{177}Hf$ for Hf standard JMC475 was 0.282145 ± 0.000008 (2SD, $n = 37$). Data were normalized relative to the accepted $^{176}Hf/^{177}Hf$ ratio for JMC475 of 0.282160 (Nowell et al., 1998). The $^{176}Hf/^{177}Hf$ of the international rock standard BHVO-1 was 0.283105 ± 0.000002 (2SD, $n = 5$), in agreement with Weis et al. (2007) (0.283106 ± 0.000012). Total analytical blanks for Hf isotopes were below 55 pg. The potential problem about Hf isotope analysis using Teflon-beaker dissolution method may come from the incomplete dissolution of zircons. Therefore, reproducibility was checked by analysing one or two replicates of the same samples on different powders in each sample batch with sample SiO_2 ranging from 48.4 wt% to 72.5 wt% (given in supplements). The reproducibility is <66 ppm and <92 ppm for Nd and Hf isotopes (in supplements), respectively. Analytical artifacts are highly unlikely in this study because granite samples have reasonably consistent zircon $\varepsilon_{Hf}(t)$ and bulk-rock $\varepsilon_{Hf}(t)$ values while the gabbronorite has a big contrast between them, which conflicts with outcomes of incomplete dissolution (see Discussion 6.1).

4.3. Mg isotope analysis

Mg isotopes were measured on a Nu Plasma II MC-ICP-MS at University of Washington, Seattle, following Teng et al. (2015). Three standards, Kilbourne Hole (KH) olivine, San Carlos (SC) olivine, and seawater, were processed together with samples for each batch of column chemistry. ^{26}Mg, ^{25}Mg and ^{24}Mg were measured simultaneously with the standard-sample bracketing protocol. Magnesium isotopic results are reported in δ notation in per mil relative to DSM-3: $\delta^{26}Mg\ (‰) = [(^{26}Mg/^{24}Mg)_{sample}/(^{26}Mg/^{24}Mg)_{DSM\text{-}3}\text{–}1] \times 1000$. Three in-house standards: KH olivine, SC olivine and seawater, yielded average $\delta^{26}Mg$ values of -0.25 ± 0.03 ($n = 3$), -0.25 ± 0.04 ($n = 3$), and -0.84 ± 0.03 ($n = 6$), respectively, which agree with previously reported values (Teng et al., 2015).

4.4. Zircon U-Pb isotope dating and Rare Earth Element

Zircon U-Pb isotope compositions and trace elements were simultaneously measured on an Agilent 7500a Q-ICP-MS equipped with a GeoLas 2005 at China University of Geosciences, Wuhan (CUGW) and on an Agilent 7500a Q-ICP-MS equipped with a UP-193 solid-state laser at China University of Geosciences, Beijing (CUGB). Procedures are similar to those by Liu et al. (2008a,b, 2010) and Song et al. (2010). At CUGW, a small amount of nitrogen was added into the argon + helium make-up gas in order to improve the precision and decrease the detection limit. The laser beam was set 32 μm. Each analysis incorporated 20–30 s of background acquisition and 50 s of data acquisition. Off-line integration of background and peak signals, drift correction, quantitative calibration for trace element analysis and U-Pb dating were performed using in-house software ICPMSDataCal provided by the lab (Liu et al., 2010). Trace element concentrations were calibrated using internal standard free method. The average analytical error ranges from ±10% for light rare earth elements (LREE) to ±5% for other trace elements. Zircon 91500 was used as the external standard and analysed twice every 5 samples throughout the analytical session. Standard silicate glass NIST SRM 610 was run every ten samples to correct for instrumental sensitivity drift and mass discrimination for the trace elements. Age calculations and Concordia plots were made using Isoplot (Ludwig, 2003). The obtained mean $^{206}Pb/^{238}U$ ages for 91500 and GJ-1 are 1062.4 ± 0.8 Ma (2σ, $n = 129$) and 599.8 ± 0.6 Ma (2σ, $n = 79$), respectively. These results are consistent with the recommended values (Wiedenbeck et al., 1995; Jackson et al., 2004). At CUGB, the procedure of laser sampling is 5 s pre-ablation and 45 s sampling ablation. The counting time for U, Th, Pb is 20 ms, and is 15 ms for other elements. Isotopic ratios and element concentrations of zircons were calculated using GLITTER (ver. 4.4, Macquarie University). Zircon standard 91500, TEMORA and NIST 610 were used during the analytical session. The obtained mean $^{206}Pb/^{238}U$ ages for 91500 are 1062.6 ± 3.3 (2σ, $n = 22$). Temora yielded apparent $^{206}Pb/^{238}U$ ages of 417.7 ± 2.4 Ma (2σ, $n = 8$), consistent with the recommended value (416.75 ± 0.24 Ma, Black et al., 2003). Concordia ages and diagrams were obtained using Isoplot/Ex (3.0) (Ludwig, 2003).

4.5. Zircon Hf isotopes

Zircon *in situ* Hf isotope analysis was done directly on top of the same pits as for U-Pb age dating using a Neptune MC-ICP-MS equipped with a 193 nm laser, at the Institute of Geology and Geophysics, Chinese Academy of Sciences in Beijing, following Wu et al. (2006). Zircons with <10% discordancy between $^{207}Pb/^{235}U$ and $^{206}Pb/^{238}U$ were analysed for Hf isotopes. The interference of ^{176}Yb on ^{176}Hf was calculated by measuring the weighted mean mass bias (β_{Yb}) for the same spot with $^{176}Yb/^{172}Yb = 0.5887$ in order to obtain precise correction for Yb interference on Hf (Wu et al., 2006). The laser beam size was set 44 μm. Zircon standard GJ-1 and Mud Tank were measured every ten samples to monitor the instrument stability. The analyses for GJ-1 (0.281998 ± 0.000016, 2σ, n = 62) and Mud Tank (0.282497 ± 0.000028, 2σ, n = 60) agree with the recommended values within 2σ error (GJ-1, 0.282015 ± 0.000019, Elhlou et al. (2006); Mud Tank, 0.282507 ± 0.000006, Yuan et al., 2008). The reference zircon Temora with high $^{176}Yb/^{177}Hf$ ratios (0.036 ± 0.020, 2σ, n = 12) gave 0.282685 ± 0.000032 (2σ, n = 12), which are identical to 0.282680 ± 0.000031 by Woodhead and Hergt (2005) and Wu et al. (2006).

5. RESULTS

5.1. Major and trace element compositions of bulk rocks

Major and trace element data are given in Table 2. Granite samples have high SiO_2 (70–72.5 wt%), low TiO_2

Table 2
Major and trace elements of Kekeli samples.

	QL10-014 Granite	QL10-015 Granite	QL10-023 Diorite	QL10-024 Diorite	QL10-027 Diorite	QL10-020 Cumulate	QL10-021 Cumulate	QL10-022 Cumulate	QL10-025 Cumulate	QL10-026 Gabbronorite
SiO_2	70	72.5	55.9	60.1	60.8	47.1	51.1	45.2	46.6	48.4
TiO_2	0.45	0.33	0.78	0.64	0.73	1.29	0.92	1.91	1.1	3.02
Al_2O_3	14.1	13.6	17.3	15.5	15.8	11.4	16.1	10.6	15.45	15.2
Fe_2O_3	0.66	0.59	2.55	1.49	1.31	4.22	3.65	5.48	2.54	3.97
FeO	2.32	1.64	4.87	4.57	4.65	9.8	5.72	11.3	7.48	8.76
MnO	0.053	0.044	0.13	0.11	0.093	0.29	0.19	0.31	0.16	0.21
MgO	1.52	1.2	3.07	3.27	3.1	6.44	4.22	7.25	11.4	4.38
CaO	1.74	1.67	7.12	4.21	2.95	12.1	8.93	11.9	8.88	7.54
Na_2O	2.9	2.56	3.25	2.8	3.78	1.78	2.82	1.11	2.23	3.19
K_2O	4.53	4.17	2.62	4.73	3.77	1.06	3.31	1.15	0.9	2.72
P_2O_5	0.1	0.082	0.52	0.4	0.5	2.21	1.01	0.92	0.17	1.2
LOI	1.39	1.39	1.37	1.62	1.93	1.14	1.34	1.59	2.23	0.4
Total	98.37	98.39	98.11	97.82	97.48	97.69	97.97	97.13	96.91	98.59
A/CNK	1.10	1.15	0.82	0.89	1.01	0.44	0.66	0.43	0.74	0.69
	1.56	1.63	0.81	1.69	1.00	0.60	1.17	1.04	0.40	0.85
Li	34.6	44.8	6.53	15.4	18	8.1	6.22	6.37	10.6	17.5
Sc	9.47	8.47	17.5	16.3	18.1	26	22.2	42.7	25.1	28.4
Cr	27.4	15.9	16.8	36.8	37.2	22.9	17.8	48.1	50.6	13.8
Co	5.69	2.86	17.6	16.2	14	34.2	24.6	36.9	55.6	26.8
Ni	10.1	9.21	7.14	9.13	6.9	15.7	11.5	14.6	23.5	10.4
Ga	19.7	17.2	21.6	19	19.5	25	21.1	27	15.4	23.5
Rb	207	186	89.1	168	165	24.2	97.2	21.1	36.3	94.2
Sr	98.2	81.9	866	607	450	450	860	461	214	430
Y	44.3	40.8	28.8	24.8	32.6	71.7	38.1	83.6	21.4	55.5
Zr	237	159	232	276	274	834	311	512	103	209
Nb	19.7	13.1	16.2	17	19	25	14.9	53	6.92	21.9
Ba	612	470	1010	1270	1010	101	2010	91	275	2000
La	49.4	32.7	40.1	57.4	101	318	122	265	12.2	62.6
Ce	99.8	64.5	98.1	110	178	589	229	439	27	134
Pr	12.5	7.97	14	13.6	20.6	65.1	28	50.3	3.92	18.5
Nd	46.7	29.4	58.1	51.6	75.1	225	109	184	17.6	78.7
Sm	9	6.01	10.9	9.42	12.9	32.6	19.2	32.7	4.09	15.5
Eu	1.05	0.98	2.59	2.29	2.86	7.34	3.75	6.37	1.29	4.33
Gd	8.24	5.83	8.9	7.79	10.5	26.5	15.5	26.5	4.11	13.7
Tb	1.39	1.14	1.23	1.06	1.39	3.24	1.93	3.69	0.68	2.04
Dy	8.06	7.24	6.06	5.11	6.82	14.8	8.69	18	4.09	11.5
Ho	1.59	1.47	1.04	0.91	1.15	2.56	1.41	3.09	0.83	2.16
Er	4.42	4.21	2.69	2.37	3.06	6.9	3.48	8.1	2.27	5.67
Tm	0.67	0.66	0.38	0.34	0.44	1	0.47	1.15	0.34	0.79
Yb	4.28	4.29	2.45	2.19	2.77	6.72	2.99	7.49	2.19	4.98
Lu	0.63	0.64	0.38	0.34	0.41	1.07	0.47	1.09	0.33	0.75
Hf	7.84	5.26	6.24	7.24	7.29	20.7	7.92	14.5	3.13	5.88
Ta	1.72	1.27	0.85	1.12	1.2	1.56	0.67	4.69	0.43	1.22
Pb	27.1	21.4	26.4	52.2	17.8	46.1	64.2	17.2	7.06	9.77
Th	25.8	12	6.79	18.2	27.8	82.8	17.3	72.6	2.51	4.6
U	5.12	2.84	3.66	4.53	4.94	21.5	5.13	13.1	0.61	0.89

(0.45–0.73 wt%), and high K_2O/Na_2O (1.56–1.63). Negative Eu anomalies are significant (0.37–0.50, Fig. 3a) and negative Sr and Ti anomalies are the largest among all samples (Fig. 3b). Diorites have lower SiO_2 (55.9–60.8 wt%), higher TiO_2 (0.64–0.78 wt%), and lower K_2O/Na_2O (0.81–1.69). Eu-Pb-Ti anomalies in the diorite are smaller than in the granite (Fig. 3b). Compared to granite and diorite samples, the cumulates have lower SiO_2 (45.2–51.1 wt%), higher TiO_2 (0.92–1.91 wt%), and lower K_2O/Na_2O (0.40–1.17). Eu-Pb-Ti anomalies in the cumulates are small (Fig. 3c, d). The gabbronorite exhibits to some extent dual signatures characterized by enrichment in both compatible and incompatible elements. It has high contents of $FeO_T + MgO$ (16.71 wt%), TiO_2 (3.02 wt%), $K_2O + Na_2O$ (5.91 wt%), LREEs and HFSEs (Fig. 3c, d) and low contents of Ni and Cr (e.g. Ni:10.4 ppm, Cr:13.8 ppm, Table 2). These features indicate that the gabbronorite precipitated from an evolved magma.

5.2. Sr-Nd-Pb-Hf-Mg Isotope compositions of bulk rocks

Bulk-rock Sr-Pb-Nd-Hf-Mg isotope data are given in Table 3. In the following discussion, $I_{Sr,}$ $Pb_{(i),}$ $\varepsilon_{Nd}(t)$ and $\varepsilon_{Hf}(t)$ refer to the age (500 Ma) corrected values, whereas ε_{Nd} and ε_{Hf} refer to the present-day values.

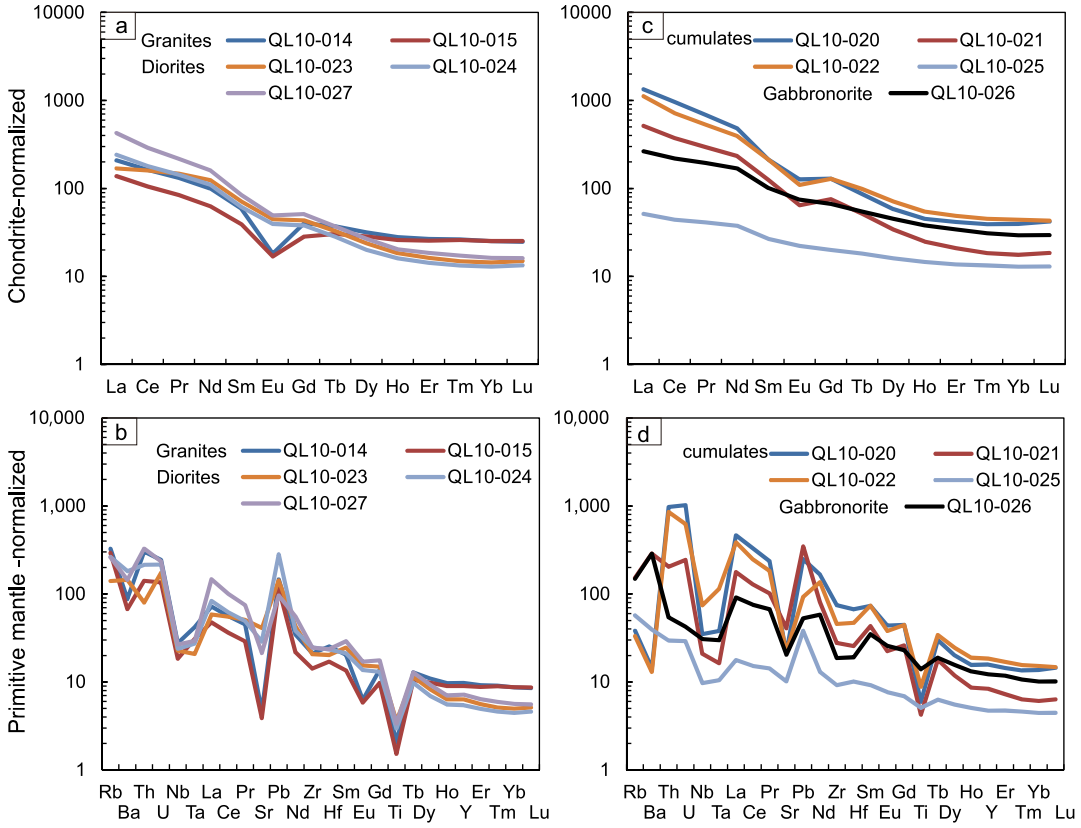

Fig. 3. Chondrite-normalized (Sun and McDonough, 1989) rare earth element (REE) (a, c) and primitive mantle-normalized (Sun and McDonough, 1989) multi-element (b, d) patterns for Kekeli samples.

The gabbronorite has the most depleted Hf isotope compositions with $\varepsilon_{Hf}(t)$ of +25.7 at $\varepsilon_{Nd}(t)$ of −1.8, thus Nd and Hf isotopes are significantly decoupled. The cumulates have less decoupled Nd-Hf isotopes with $\varepsilon_{Hf}(t)$ values of +5.2 to +8.0 at $\varepsilon_{Nd}(t)$ values of +0.2 ∼ +0.6. The host diorite has $\varepsilon_{Nd}(t)$ values of +0.2 ∼ +0.7 and $\varepsilon_{Hf}(t)$ values of +3.6 ∼ +5.6, overlapping the cumulate values. The granite samples have the lowest $\varepsilon_{Nd}(t)$ values (−5.9 ∼ −6.6) and the lowest $\varepsilon_{Hf}(t)$ values (−5.0 ∼ −2.0) (Table 3). The cumulates and host diorites have similar I_{Sr} values (0.707–0.708). The gabbronorite has slightly radiogenic Sr isotopes (I_{Sr} of 0.710) and the granite has the most radiogenic Sr isotopes (I_{Sr} of 0.733–0.740). All the samples have similar and radiogenic Pb isotopes ($^{206/204}Pb = 18.497–19.477$). Overall, bulk-rock $\varepsilon_{Hf}(t)$ values define a broad negative trend with SiO_2 (and broad positive correlations with FeO, MgO and MnO) with the granite being slightly negative and other samples largely positive (Fig. 4a). Importantly, the bulk-rock $\varepsilon_{Hf}(t)$ defines a tight positive correlation with TiO_2 ($R^2 = 0.94$, Fig. 4b). The entire sample suite exhibits varying degrees of bulk-rock $\varepsilon_{Hf}(t) - \varepsilon_{Nd}(t)$ decoupling, increasing from the granite to the gabbronorite (Fig. 4c).

The $\delta^{26}Mg$ values range from −0.29‰ to −0.12‰, with the gabbronorite and cumulates having relatively heavier Mg isotopic compositions than the granite (Fig. 5a). The $\delta^{26}Mg$ values display positive trends with Hf isotopes and TiO_2, but have a negative trend with SiO_2 (Fig. 5).

5.3. Zircon trace elements and geochronology

Zircon U-Pb age data, rare earth elements (REE), *in situ* Hf isotopes and standard data are reported in the supplements.

5.3.1. Granite

The granite samples contain magmatic zircons as well as inherited cores with magmatic overgrowth rims (Fig. 6). They exhibit various internal structures (Fig. 6). Some of them display magmatic oscillatory zoning while others show homogenous, core-mantle-rim texture, planar banding, patchy, fir-tree or radial sector zoning. The magmatic zircons display a typical zircon REE pattern (Fig. S1), e.g., the steeply-rising slope from LREE to HREE with a positive Ce-anomaly and negative Eu-anomaly is consistent with an igneous origin. Whereas some grains show LREE enrichment, decreased Ce anomaly or flat HREE patterns (Fig. S1). Enriched LREEs are typical for hydrothermal zircons (Hoskin, 2005) or the analysis of apatite inclusion. Hydrothermal alteration can cause Pb loss or Lu loss in zircon without affecting $^{176}Hf/^{177}Hf$ ratios. It affects calculated initial $^{176}Hf/^{177}Hf$ values because of the lowered Lu/Hf ratios (Gerdes, 2009); however, this influence is negligible due to the very low Lu/Hf ratios in zircon. To avoid potential problem in comparing zircon Hf isotopes to whole rock Hf isotopes, we filtered zircons by using zircon REEs:

Table 3
Bulk-rock Sr-Nd-Hf-Pb-Mg isotopic data and zircon weighted-mean εHf(t) of samples in Kekeli. Age corrected to 500 Ma.

	QL10-14 Granite	QL10-15 Granite	QL10-23 Diorite	QL10-24 Diorite	QL10-27 Diorite	QL10-20 Cumulate	QL10-21 Cumulate	QL10-25 Cumulate	QL10-26 Gabbronorite
$^{176}Lu/^{177}Hf$	0.011	0.017	0.008	0.007	0.008	0.007	0.008	0.015	0.018
$^{176}Hf/^{177}Hf$	0.282520	0.282489	0.282675	0.282689	0.282646	0.282763	0.282695	0.282796	0.283364
2σ	0.000005	0.000007	0.000009	0.000008	0.000007	0.000006	0.000009	0.000007	0.000009
$\varepsilon_{Hf}(t)$	−2.0	−5.0	4.4	5.6	3.6	8.0	5.2	6.7	25.7
Zirocn average $\varepsilon_{Hf}(t)$	−5.9	−6.5	−1.2	−0.4	−0.7	N/A	−2.7	5.4	1.8
Ti-in-zircon (°C)*	782	783	693	744	751		733	736	715
Zr-WR temperature (°C)**	822	795	747	787	805	656	712	636	679
$^{147}Sm/^{144}Nd$	0.116938	0.124039	0.113837	0.110773	0.104227	0.087916	0.106882	0.141007	0.119506
$^{143}Nd/^{144}Nd$	0.512067	0.512057	0.512371	0.512359	0.512365	0.512286	0.512369	0.512483	0.512289
2σ	0.000011	0.000014	0.000007	0.000007	0.000008	0.000011	0.000009	0.000009	0.000005
$\varepsilon_{Nd}(t)$	−5.9	−6.6	0.2	0.2	0.7	0.2	0.6	0.6	−1.8
$\delta^{26}Mg$ (DSM3)	−0.27	−0.29	−0.23	−0.24	−0.17	−0.12	−0.25	−0.24	−0.16
2σ	0.06	0.06	0.10	0.10	0.10	0.10	0.10	0.10	0.10
$^{87}Rb/^{86}Sr$	5.97	6.43	0.29	0.78	1.04	0.15	0.32	0.48	0.62
$^{87}Sr/^{86}Sr$	0.77537	0.78554	0.70999	0.71295	0.71428	0.70929	0.71036	0.71171	0.71441
2σ	0.00007	0.00010	0.00009	0.00009	0.00009	0.00010	0.00006	0.00008	0.00008
I_{Sr}	0.733	0.740	0.708	0.707	0.707	0.708	0.708	0.708	0.710
$^{206}Pb/^{204}Pb$	19.960	19.608	19.362	19.142	20.837	21.051	18.888	19.195	19.106
2σ	0.001	0.001	0.001	0.002	0.001	0.002	0.001	0.001	0.002
$^{207}Pb/^{204}Pb$	15.712	15.688	15.688	15.673	15.773	15.783	15.661	15.672	15.668
2σ	0.001	0.001	0.001	0.001	0.001	0.002	0.001	0.001	0.001
$^{208}Pb/^{204}Pb$	39.795	38.678	38.503	38.730	40.418	41.175	38.534	39.101	39.229
2σ	0.004	0.004	0.004	0.004	0.004	0.005	0.003	0.004	0.003
$^{208}Pb/^{204}Pbi$	38.30	37.80	38.10	38.18	37.96	38.35	38.11	38.54	38.49
$^{207}Pb/^{204}Pbi$	15.66	15.65	15.65	15.65	15.69	15.65	15.64	15.65	15.64
$^{206}Pb/^{204}Pbi$	19.03	18.96	18.68	18.72	19.48	18.77	18.50	18.77	18.66

Ti-in-zircon (°C)*: Ferry and Watson, 2007
Zr-BR temperature (°C)**: Miller et al., 2003

CHUR: $^{176}Hf/^{177}Hf = 0.282785$, $^{176}Lu/^{177}Hf = 0.0336$, $^{143}Nd/^{144}Nd = 0.512630$, $^{147}Sm/^{144}Nd = 0.1960$, Bouvier et al. (2008); $\lambda^{176}Lu = 1.867E\text{-}11\ yr^{-1}$, Söderlund et al. (2004); $\lambda^{147}Sm = 6.54E - 12\ yr^{-1}$, Lugmair and Marti (1978); $\lambda^{87}Rb = 1.42 E - 11\ yr^{-1}$, Steiger and Jäger, 1977; $\lambda^{238}U = 1.55 \times 10\text{–}10\ yr^{-1}$, $\lambda^{235}U = 9.85 \times 10\text{–}10\ yr^{-1}$, $\lambda^{232}Th = 4.95 \times 10\text{–}11\ yr^{-1}$, Jaffey et al., 1971.

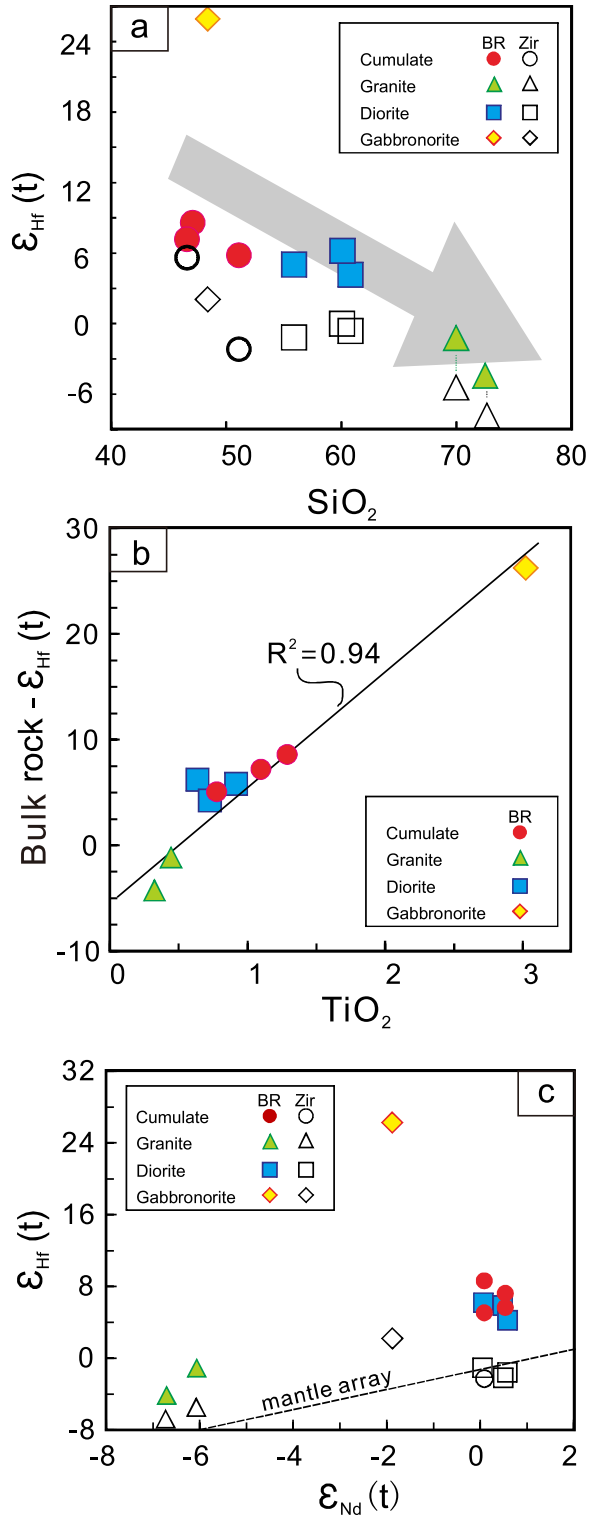

Fig. 4. Bulk-rock (BR, solid symbols) and zircon (open symbols) Hf isotope variation against SiO_2 (a) and TiO_2 (b), showing significant positive correlation of bulk-rock $\varepsilon_{Hf}(t)$ and TiO_2(-$R^2 = 0.94$); (c) bulk-rock and zircon Hf isotope variation against bulk-rock Nd isotopes, showing bulk-rock Hf-Nd isotope decoupling, but zircon Hf isotopes are coupled with bulk-rock Nd isotopes. Error bars for bulk rock values are smaller than symbols.

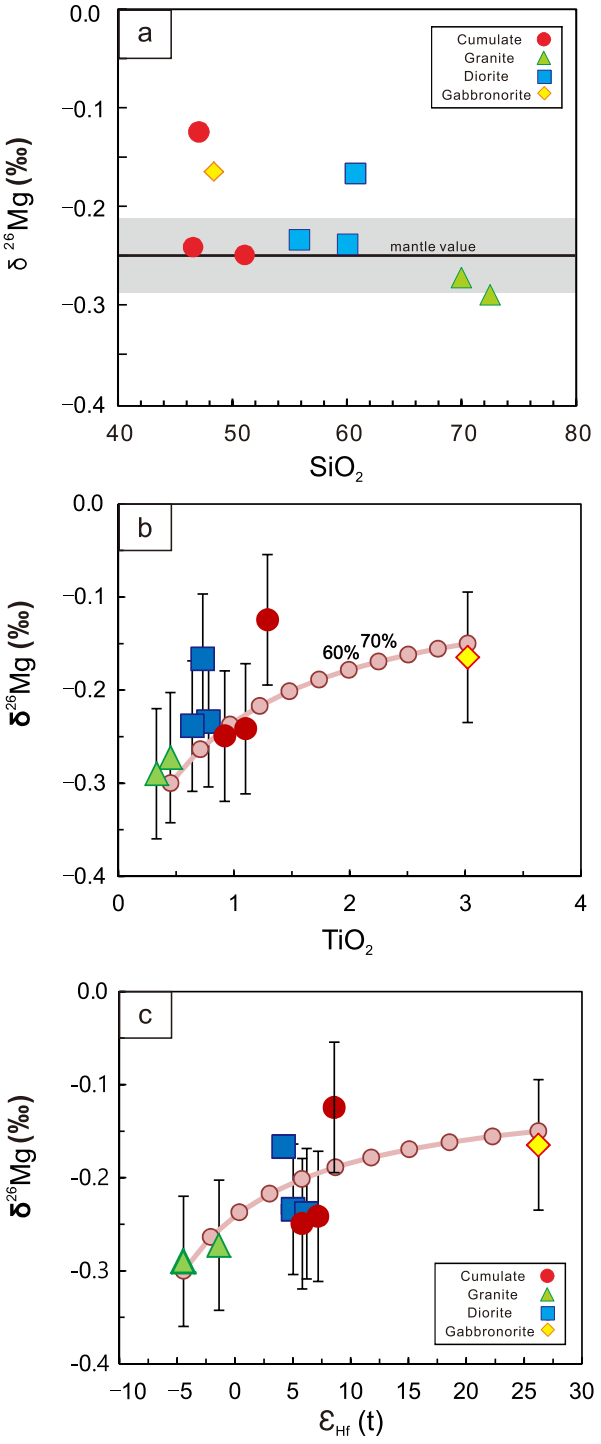

Fig. 5. Bulk-rock $\delta^{26}Mg$ variation against SiO_2, TiO_2 and $\varepsilon_{Hf}(t)$. (b, c) The samples plot along the apparent mixing trend with the granite and the gabbronorite as two endmembers.

those having high LREEs were not analysed for Hf isotopes. The varying features indicate complex histories or origins of these zircons. Th/U ratios range from 0.1 to 1.61 with the metamorphic cores having Th/U < 0.1 (Table S1).

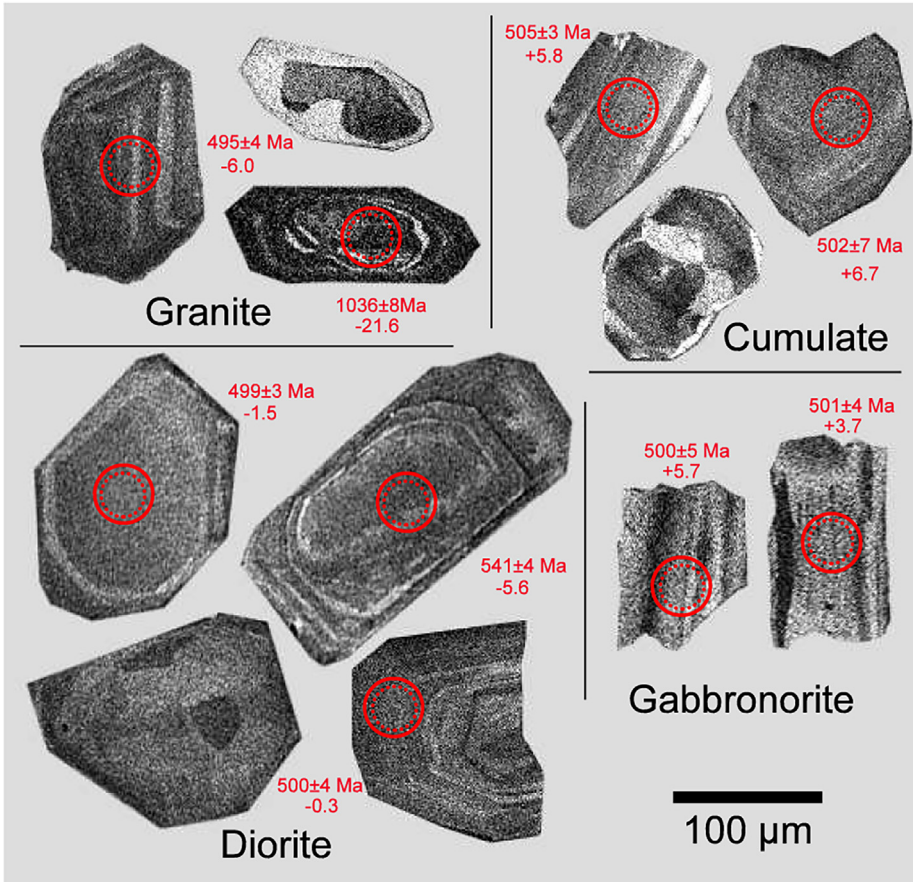

Fig. 6. Zircon cathodoluminescence (CL) images. Dash circles represent zircon U-Pb dating. Solid circles represent Hf isotope analysis.

Zircon rims with oscillatory zoning yielded the crystallization age of 500.7 ± 2.1 Ma and 502.4 ± 4.0 Ma for granite samples QL10-14 and QL10-15, respectively. Two grains in QL10-14 with blurry zones and flat heavy-REEs yielded a coherent U-Pb age of ~501 Ma (Table S1). Two grains in QL10-15 with similar CL images and flat HREEs also yielded coherent U-Pb ages of ~501 Ma. Seven inherited zircon cores in QL10-15 plot along or close to the Concordia, yielding $^{207}Pb/^{206}Pb$ ages of 1317 to 2634 Ma. Such varying features in the zircon morphology and REE patterns indicate an anatexic origin for the granite.

5.3.2. Diorite and enclosed cumulates

The diorite and cumulate samples contain abundant magmatic zircons as well as minor inherited grains similar to those in the granite (Fig. 6). They are mostly fragments, homogenous or have oscillatory bands (Fig. 6), exhibiting the smallest Eu anomaly (QL10-25 Fig. S1), consistent with a small Eu anomaly in the bulk-rock REE pattern (Fig. 3). The diorite sample QL10-27 exhibits a low-grade metamorphic mineral assemblage (see above), which is reflected in the zircon REE pattern with some grains having enriched LREEs without a Ce anomaly (Fig. S1). Some zircons plot slightly off the Concordia, but the zircon populations still define a well constrained concordant age of ~500 Ma. The other diorite and cumulate samples yielded discordant ages ranging from 530 Ma to 1000 Ma overlapping those in the granite (Fig. 7). Th/U ratios range from 0.30 to 1.09 in the diorite zircons and from 0.27 to 1.59 in the cumulate zircons (Table S1).

5.3.3. Gabbronorite

Zircons in the gabbronorite are mostly fragments of >100 μm size and exhibit oscillatory zoning or planner banding (Fig. 6). All the grains have consistent and typical magmatic REE patterns with the steeply-rising slope from LREE to HREE, a positive Ce-anomaly and negative Eu-anomaly (Fig. S1). They give a concordant age of 500.1 ± 1.9 Ma. Notably, there are no old inherited ages found in the gabbronorite (Fig. 7). The Th/U ratios in the gabbronorite zircons range from 0.27 to 1.59.

5.3.4. Summary

The granite contains abundant metamorphic zircons inherited from the granulite or eclogite component. The diorite and enclosed cumulates have zircon populations comparable to those in the granite. Zircons in the gabbronorite exhibit oscillatory zoning typical of magmatic rocks. Zircons in granite, diorite, cumulates and gabbronorite have Th/U ratios dominantly >0.2 (supplements), consistent with a magmatic origin (Hoskin and Schaltegger, 2003). All the samples have identical ages within error:

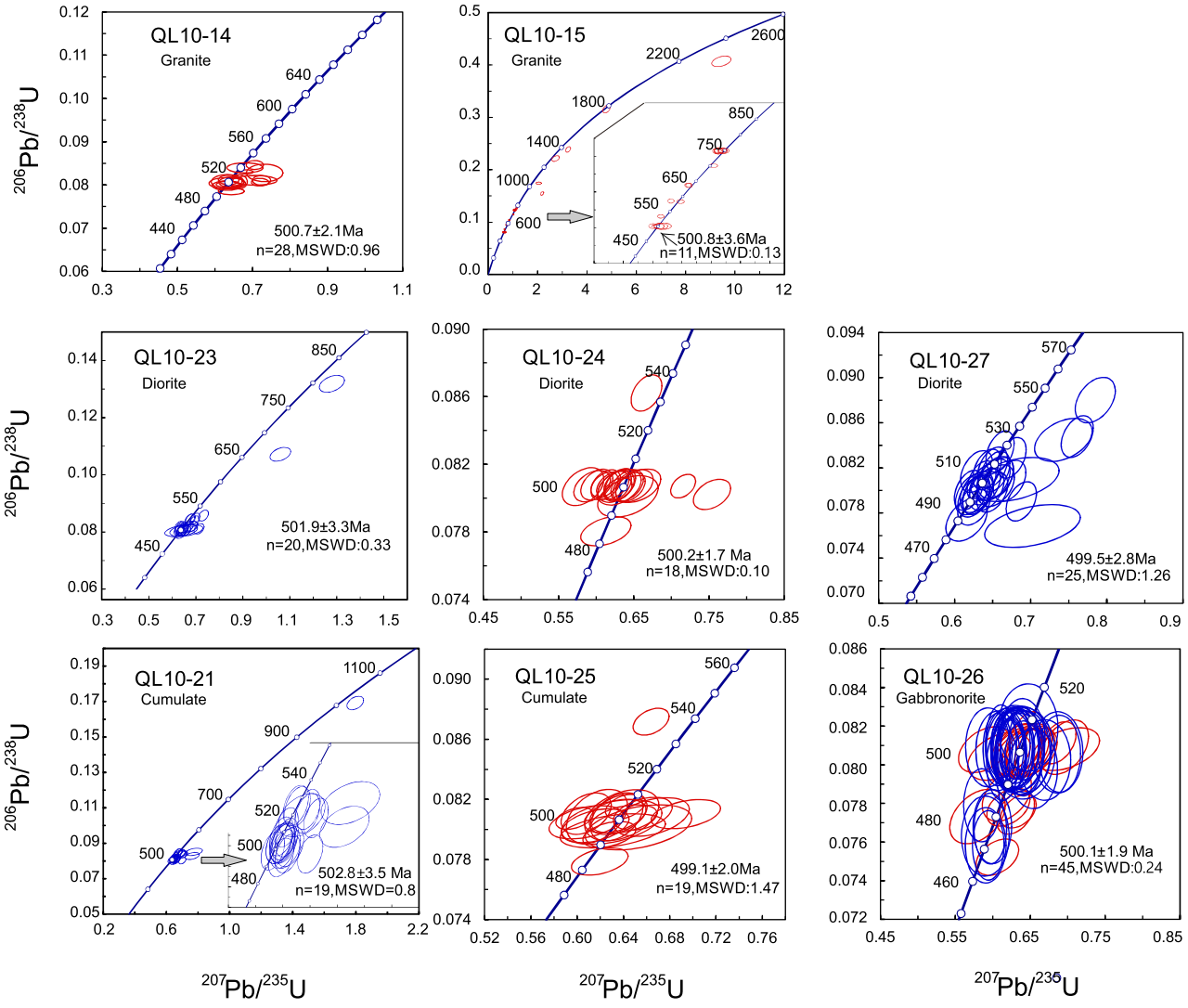

Fig. 7. Zircon U-Pb Concordia Plots. Data in red were obtained at CUGW. Data in blue were obtained at CUGB.

~500 Ma, representing the emplacement age of the batholith.

5.4. Zircon *in situ* Hf isotopes

Zircons with >90% concordance and typical magmatic REEs were analyzed for Hf isotopes. The two granite samples yielded the $\varepsilon_{Hf}(t)$ range of −9.2 to −2.4 and −8.9 to −2.1, respectively, with the old core having $\varepsilon_{Hf}(t)$ of −21.6 (Table S2). They define the lowest weighted mean values of -6.2 ± 1.8 and -5.6 ± 0.8 (Fig. 8), slightly lower than their bulk-rock $\varepsilon_{Hf}(t)$ values (−5.0 to −2.0). Given the obvious inherited cores with very negative $\varepsilon_{Hf}(t)$ values and spread discordant ages, we consider that the $\varepsilon_{Hf}(t)$ in the zircons and their bulk-rock are reasonably consistent. It also suggests that the inherited zircon cores contribute little to the bulk-rock Hf isotopes. The three diorite samples gave the $\varepsilon_{Hf}(t)$ range of −8 to +1.3, −0.9 to +1.6 and −6.7 to +1.7, respectively, yielding higher weighted mean values from -0.8 ± 2.2 to $+0.1 \pm 0.66$ (Fig. 8). These zircon Hf isotope compositions differ from their bulk-rock $\varepsilon_{Hf}(t)$ range (+3.6 to +5.6) (Fig. 9a). The entire range of $\varepsilon_{Hf}(t)$ values for the cumulate gave −6.3 to +1.3 and +4.0 to

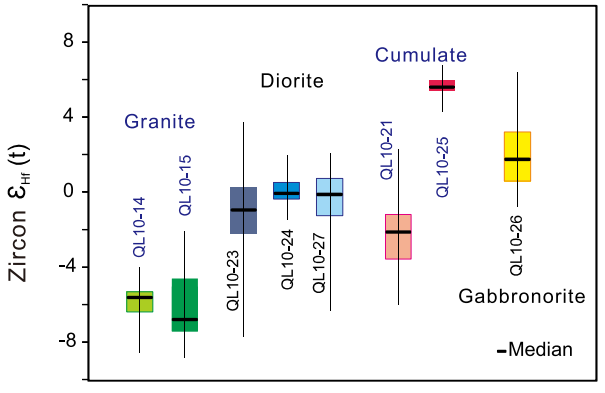

Fig. 8. Box and whisker plot for zircon $\varepsilon_{Hf}(t)$ values.

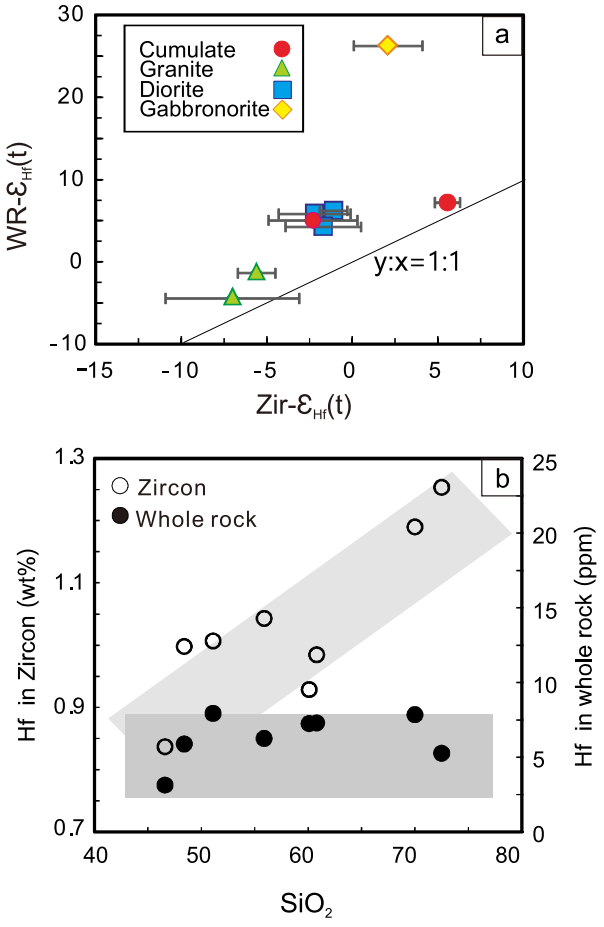

Fig. 9. (a) Showing the discrepancy between zircon and bulk-rock Hf isotopes. If they are consistent, they should plot on the y = x line. (b) Showing zircon Hf content increases whereas bulk-rock Hf content remains constant with increasing bulk-rock SiO_2.

+6.5, with weighted mean of -2.4 ± 1.6 and $+5.7 \pm 0.6$, overlapping their bulk rock $\varepsilon_{Hf}(t)$ values (+5.2 to +8.0) and similar to those of the diorite (Figs. 8, 9a). The gabbronorite has a range of −1.1 to +6.0 in zircon $\varepsilon_{Hf}(t)$ with the average of $+1.8 \pm 1.6$, which differs significantly from its very high bulk-rock value (+25.7) (Fig. 9a).

The average zircon $\varepsilon_{Hf}(t)$ values yield a broad negative trend with SiO_2 (Fig. 4a). Most of the average zircon $\varepsilon_{Hf}(t)$ values shift towards lower values than their corresponding bulk-rock $\varepsilon_{Hf}(t)$ values (Fig. 4a, 9a). While the zircon $\varepsilon_{Hf}(t)$ averages show coupling with the bulk-rock $\varepsilon_{Nd}(t)$, the bulk-rock $\varepsilon_{Hf}(t)$ values are mostly decoupled from the bulk rock $\varepsilon_{Nd}(t)$s (Fig. 4c). The discrepancy between zircon *in situ* $\varepsilon_{Hf}(t)$ values and bulk rock $\varepsilon_{Hf}(t)$ values generally increase from the granite (reasonably consistent) to the gabbronorite (large contrast) (Fig. 9a), which is apparently not resulted from incomplete dissolution of zircons in felsic rocks (as discussed below).

6. DISCUSSION

The data demonstrate significant Hf isotope discrepancies between bulk rocks and their constitute zircons and pronounced bulk rock Nd-Hf isotope decoupling. Before we investigate the possible mechanism that may produce the discrepancy, we first validate the discrepancy and discuss variations in zircon Hf isotopes. The implication of this study is evaluated at the end.

6.1. Discrepancy between bulk-rock $\varepsilon_{Hf}(t)$ and zircon $\varepsilon_{Hf}(t)$

The discrepancy between bulk-rock and zircon Hf isotopes may reflect several scenarios: (1) incomplete bulk-rock sample dissolution; (2) inaccurate interference correction; and (3) zircon disturbance or re-opening of the Lu-Hf system in whole rock samples. However, none of them can account for the observation in this study.

Blichert-Toft et al. (2004) compared bomb-dissolved and beaker-dissolved solutions and found that the later has much lower Hf contents than the former. This is considered that some Hf-rich minerals are not dissolved in beaker-dissolved solutions, e.g., zircon or baddeleyite. Tappe et al. (2007, 2008) later compared two methods and found that identical Hf isotopes were obtained in both beaker-dissolved solutions and bomb-dissolved solutions. The potential effect of incomplete digestion of zircons has been examined by Huang et al. (2014) and is further evaluated here. Beaker digestion method for isotope analysis cannot digest zircons completely and leave the zircon-rich granites more suspect than the mafic gabbronorite. As zircon has very low Lu/Hf ratio, it thus has unradiogenic Hf isotopes than the non-zircon phases in the rock. Incomplete digestion would theoretically produce more radiogenic Hf isotope compositions and low Hf concentration in the solution. This is essentially the same process as zircon disequilibrium melting (Gerdes, 2012; Tang et al., 2014; Wang et al., 2017). If more zircons are dissolved, low $^{176}Hf/^{177}Hf$ and high Hf contents in melts are theoretically expected while high $^{176}Hf/^{177}Hf$ should associate with low Hf contents when less zircons are dissolved (Farina et al., 2014). But measured $^{176}Hf/^{177}Hf$ ratios do not correlate with Hf contents in this study (see Fig. S2 in supplements). Importantly, digestion using Teflon beakers can dissolve zircons to some extent, and thus the Hf in the dissolved portions of zircons will enter the solution accordingly especially given much smaller rock powder particle size, which allows zircon fragments in the rock-powders well exposed with enhanced surface areas and facilitated digestion and dissolution (Huang et al., 2014). Moreover, inherited/captured zircons in the granites are usually overgrown by newly formed rims whose composition represents that of the magma. Incomplete digestion of these zircons should have yielded consistent results because zircon rims would have the same or similar Hf isotopes as the melt (approximated by the bulk-rock). Despite all the above, the good reproducibility of bulk rock Hf isotopes for samples having SiO_2 in the range of 48.4–72.5 wt% (in supplements) demonstrate that these data are reliable. Moreover, the granite with abundant zircons has reasonably consistent Hf isotopes in zircons and bulk rocks while gabbronorite with less zircons has a big contrast between them (see above). This also rules out analytical artifact due to incomplete dissolution.

The concerns regarding the accuracy of correction for the isobaric interference of ^{176}Yb on ^{176}Hf for *in situ* zircon Hf isotopes can also be ruled out. Our samples have $^{176}Yb/^{176}Hf$ ratios generally between 0.002 and 0.07 with 90% of them <0.036 (73% of them <0.02 and 92% of them <0.04). Among the three reference zircons (GJ-1, Mud Tank 1 and Temora), only Temora has high $^{176}Yb/^{176}Hf$ ratios (0.036 ± 0.020, comparable to the values in these zircons. The standard Temora analyses in the lab throughout the session during which we analyzed samples yielded $^{176}Hf/^{177}Hf$ ratio of 0.282685 ± 0.000032, agreeing well with the published value 0.282680 ± 0.000031 (Wu et al., 2006). Notably, any under- or overcorrection for Yb interference on ^{176}Hf would produce correlations between $^{176}Yb/^{177}Hf$ and $^{176}Hf/^{177}Hf$ (Fisher et al., 2014; Farina et al., 2014). Such correlations are not observed in this study. Besides, zircon Hf isotopes and whole rock Nd isotopes plot along the terrestrial array (Fig. 4c). This is important as such a correlation is geologically real and cannot be explained by analytical artifact. Therefore, our data cannot be explained by isobaric interference.

Non-zero-aged Pb loss in zircons or re-opening of Lu-Hf systems can also cause the discrepancy. But this is unlikely here. Lead loss can affect the determined zircon ages without changing measured zircon Hf isotopes hence can affect calculated εHf values because of the great time-dependence of CHUR values (Guitreau et al., 2012). The problem resulting from Pb loss can be avoided by analysing Hf isotopes only using zircons with >90% Concordance and subsequently consistent Hf isotopes in whole rock and constitute zircons are obtained (Guitreau et al., 2012). In this study only zircons with >90% concordant ages were analysed for *in situ* Hf isotopes. A few grains in the granite have Th/U < 0.1 but contain similar Hf isotopes to others (Table S2). Hence, the influence of Pb loss is ruled out. Furthermore, the biggest discrepancy is observed in the gabbronorite in which all zircons are perfectly concordant (Fig. 7) and all have Th/U ratios in the range of 0.2–1.87 (Table S1), consistent with the global magmatic zircon Th/U values (Kirkland et al., 2015). Therefore, the disturbance in zircons, if any, cannot account for the discrepancy in this study. Lu-Hf system re-opening at the whole rock scale without affecting zircon Hf isotopes is also a possible factor to cause the discrepancy. This can be readily ruled out. Although the NQOB experienced multiple metamorphic events in the region (see above), the samples in this study are fresh, except some diorite show low-grade metamorphic mineral overprint. No evidence in the field or under microscope shows these samples were metamorphosed. Also, the low-grade metamorphism as observed in the diorite is not expected to have reset the Lu-Hf system.

6.2. Variations in zircon Hf isotopes

Zircon $\varepsilon_{Hf}(t)$ variations in some samples are restricted (2 epsilon units), but quite large (9 epsilon units) in other samples (Fig. 8). These observations could be caused by disequilibrium melting during the crustal anatexis (Tang et al., 2014). But disequilibrium melting is difficult to explain isotopic variations on hand-specimen scales because it assumes rapid melt extraction from the source. In this case, how zircons with varying Hf isotopes from different melt batches managed to juxtapose in a small hand specimen is a question. Disequilibrium melting is also expected to produce a correlation between Hf isotopes and Hf content, which is again not observed in this study (see Section 6.1, supplements). Moreover, it cannot explain generally less radiogenic Hf isotopes in zircons than that of the whole rock in our samples. It is more likely that the variation in zircon Hf isotopes reflect the heterogeneity resulting from an open magmatic system.

6.3. Significant Hf in non-zircon phases

As discussed above, the discrepancies between whole rocks and their constitute zircons are real. They have three important features: (1) zircon $\varepsilon_{Hf}(t)$ values are dominantly <0, whereas bulk-rock $\varepsilon_{Hf}(t)$ values are generally >0 (Fig. 4a); (2) bulk-rock $\varepsilon_{Hf}(t)$ values are decoupled from bulk-rock $\varepsilon_{Nd}(t)$ while zircon $\varepsilon_{Hf}(t)$ values are coupled (Fig. 4c); (3) bulk-rock $\varepsilon_{Hf}(t)$ values define a tight positive correlation with TiO_2 ($R^2 = 0.94$, Fig. 4b). Previous studies have suggested positive, though broad, correlations between initial Hf isotope ratio and Ti contents in zircons as a result of the increasing crustal assimilation-related cooling (Heinonen et al., 2010; Pankhurst et al., 2013). Our samples do not have such correlations.

It is important to note that bulk-rock Hf concentrations remain almost unchanged from mafic cumulates to felsic granites (Fig. 9b), whereas average Hf contents in zircons increase with increasing bulk rock SiO_2 because of increasing Kd's with increasing SiO_2 in the melt (Green, 1994). Assuming mafic lithologies contain less or even equal amounts of zircons as felsic lithologies, mass balance requires that mafic cumulates have additional phases hosting significant amounts of Hf compared to felsic hosts. Simple calculations show that 20–44% of the bulk-rock Hf is hosted in non-zircon phases (Table S3), which agrees with the estimate by Xiong et al. (2014) that zircons in some mafic rocks in Qilian area host ~30% Hf.

Potential minerals apart from zircons hosting significant Hf should be those rich in Ti. Charge and size dependent "Lattice Strain" model (Onuma et al., 1968; Wood and Blundy, 1997) predicts that Zr^{4+} and Hf^{4+} should behave similarly to Ti^{4+} because of their same charges. Partition coefficients show that Hf is compatible in Ti-rich minerals ($Kd_{Ilm} = 3.1$, Nash and Crecraft, 1985; $Kd_{Amp} = 1.87$, Hilyard et al., 2000). Zr contents in Ti-rich minerals decrease from thousands of ppm in ilmenite or titanite with generally consistent Zr/Hf ratios (37–40) to a few hundreds of ppm in amphibole with varying Zr/Hf ratios of 15–40 (Bea et al., 2006). Given the distinct mineralogy in different samples, possible Ti hosts may vary. For example, gabbronorite has up to 4.2% modal ilmenite hosting Hf. Although Cpx also contains Hf (Salters and Zindler, 1995), the leverage of Cpx on the bulk rock Hf isotopic composition is much smaller than Ilm (e.g. <1 ppm Hf in Cpx (Salters and Zindler, 1995) vs. >40 ppm Hf in Ilm (Nowell et al., 2004; Bea et al., 2006)). While in cumulates, the abundance of ilmenite is less than in the gabbronorite

and amphibole becomes the dominant Ti-rich mineral hosting Hf apart from zircons.

6.4. Ti minerals have different Hf isotope composition from zircon: magma mixing

The major mineral assemblage in the gabbronorite indicates a high crystallization temperature. Pyroxene crystallizes at >1050 °C and ilmenite crystallizes at ~1100 °C (Dick et al., 2000; Niu et al., 2002). By constrast, Ti-in-zircon temperature gives low T of 715 °C for the gabbronorite (Ferry and Watson, 2007). As for the cumulate samples, amphibole is the dominant mineral and has a crystallization temperature above 850 °C (Bogaerts et al., 2006), and Ti-in-zircon thermometer gives the highest temperatures of 693 °C (Table. 3). Given the observation that the discrepancy between zircon and bulk-rock Hf isotopes decreases from the gabbronorite to the granite (Fig. 9a), which corresponds to the decreasing contrast of crystallization temperature between Ti-rich minerals and zircon, zircons in the more mafic samples are out of equilibrium with Ti-rich minerals, e.g., zircons precipitated later at lower temperatures than Ti-rich minerals.

During magma evolution, zircon does not reach saturation at the time when ilmenite begins to crystallize. DeLong and Chatelain (1990) have inferred according to experiments, geochemistry and petrography that ilmenite crystallizes at 1100 °C from a liquid with about 4% TiO_2 and 300 ppm Zr while zircon does not precipitate until the magma cools down to 840 °C and Zr reaches 700 ppm. Furthermore, recent experiments require extremely high abundance of >3000–5000 ppm Zr to directly crystallize zircons in basaltic melts (Dickinson and Hess, 1982; Hanchar and Watson, 2003; Boehnke et al., 2013). Therefore, any zircon in mafic rocks should have actually crystallized from an evolved magma (Zheng et al., 2006; Boehnke et al., 2013). When abundant non-zircon minerals on the liquidus already crystallized, much of Zr and Hf has been partitioned into these minerals, especially Ti-rich minerals, and thus less Zr and Hf is available for zircons to form subsequently. The emplacement of the hot basaltic magma in the lower crust level can cause lower crustal melting and magma mush zone formation. While the basalt evolves, at the point of ilmenite and clinopyroxene starts crystallization, the equilibrium melt evolves towards felsic composition due to oxide fractionation/crystallization (Niu et al., 2002). These more felsic melts could be trapped, expelled out or modified by subsequent melt replenishment. When the early crystallized mafic silicates and ilmenites are still plastic before complete solidification (maybe after millions of years), they can be easily disturbed by the granitoid magma replenishment. The early formed clinopyroxene could react with the later intermediate/felsic magma as demonstrated by the amphibole-biotite rims around the crystals (Fig. 2). If the basaltic and granitic magmas are difficult to mix due to their contrasting viscosity, the relatively felsic melt resulting from ilmenite and clinopyroxene fractionation should be readily mixed with the felsic magma derived from partial melting of the lower crust because of smaller viscosity difference. In this case, zircons in the gabbronorite could actually have crystallized from the later melt mixtures and would not equilibrate in terms of isotopes with the former crystallized minerals. Hence, the discrepancy of Hf isotopes between bulk rocks and zircons could result from different timing of crystallization between Ti minerals and zircons in an open magmatic system. The discrepancy decreasing from the gabbronorite to the granite is consistent with the magma mixing processes and also is consistent with the decreasing Zr contents from the ilmenite, amphibole to biotite (thousands of ppm to a few ppm, Bea et al., 2006). We are unable to map Hf isotopes of all the possible minerals given the limited amount of samples we have at the moment, but this is our work under consideration.

The positive correlations between Mg isotope values and major elements and Hf isotopes, as shown in Fig. 5 support the mixing hypothesis. The granites have mantle-like $\delta^{26}Mg$ values, similar to other I-type granites (Liu et al., 2010). The diorite, cumulate and gabbronorite have variably higher $\delta^{26}Mg$ values than the granites, in accordance with their relatively higher TiO_2 values. Wang et al. (2014) also reported heavier Mg isotopic compositions for Ti-rich gabbro cumulates from the Dabie orogen. This enrichment of heavy Mg isotopes in high-Ti rocks could result from accumulation of Ti minerals in these rocks, as the recent study found that Ti minerals such as cumulus ilmenite has extremely high $\delta^{26}Mg$ values compared to silicate minerals (Chen et al., 2018). For example, cumulus ilmenites in gabbros (with whole rock $TiO_2 = 1.5–8$) from the Baima intrusion in China have $\delta^{26}Mg$ values as high as +1.9 (Chen et al., 2018). Whether or not the ilmenite has been isotopically equilibrated with coexisting silicate minerals is unknown, but accumulation of these high-$\delta^{26}Mg$ ilmenites in the gabbronorite provides the best explanation for the observed heavy Mg isotopic signature (Fig. 5). Our samples fit well on a mixing curve using the granite and gabbronorite as two endmembers with intermediate compositions between them (Fig. 5b, c), thus highlighting the important role of Ti-rich minerals in creating Hf-Mg isotopic heterogeneity during magma mixing.

6.5. Extremely high $\varepsilon_{Hf}(t)$ of the Ti-rich endmember?

The above mixing model suggests that the $\varepsilon_{Hf}(t)$ of some samples are very high and decoupled from the $\varepsilon_{Nd}(t)$ (Fig. 4c). The gabbronorite has the largest discrepancy in Hf isotopes between zircons and bulk-rock and biggest bulk-rock Nd-Hf isotope decoupling. To compensate the discrepancy, $\varepsilon_{Hf}(t)$ of non-zircon phases would need to be $+28 \sim +84.5$, which are conservative values assuming 30–100% Zr resides in zircon in mafic lithologies. Other more felsic samples are also significantly depleted in Hf isotopes for non-zircon phases (Table S3) because of more Zr hosted in zircons.

So far extreme Nd-Hf isotope decoupling with extreme high ε_{Hf} at a comparably unradiogenic ε_{Nd} have only been observed in the lithospheric mantle where ε_{Hf} in Cpx or Grt could be as high as $+200 \sim +2500$ at ε_{Nd} of $-20 \sim +30$ (Salters and Zindler, 1995; Bedini et al., 2002; Schmidberger et al., 2002; Simon et al., 2002, 2003;

Pearson and Nowell, 2003). The distinct sub-vertical array above the mantle Nd-Hf isotope array is unique to subcontinental lithospheric mantle (SCLM), thus Hf isotopes are a powerful tracer of lithospheric source regions in magmas (Pearson and Nowell, 2003). However, basalts with anomalous Hf isotopes derived from the SCLM have not been reported, most likely because SCLM is too refractory to melt again. Niu (2005, 2014) proposed a basal hydration weakening model to explain the eastern China lithosphere thinning in which the deeply subducted slab transported tremendous amount of water to the base of the SCLM and eventually converted SCLM to convective asthenosphere while producing basalt with enriched signature (Niu, 2005 and reference therein). The very limited data for lithospheric mantle underneath the Qilian Orogenic belt show that the Archean subcontinental lithospheric mantle had multiple refertilization and metasomatism events (Xiong et al., 2014; 2015). Garnets in pyroxenite have enormously high ε_{Hf} (>+200) and reconstructed bulk rock ε_{Hf} (500 Ma) values for such pyroxenite are +14.5 to +22.4 at ε_{Nd}(500 Ma) of −3.8 to −3.7 (Xiong et al., 2014). The mantle could have obtained the decoupled Nd-Hf isotopes via heavy metasomatism by which the slab-derived fluids modified the Sr and Nd isotopes without changing the Hf isotopes and simultaneously caused the enrichment of LREEs and depletion in HFSE (Xiong et al., 2014). The gabbronorite has similar Nd and Hf isotopes to these pyroxenites ($\varepsilon_{Nd}(500) = -1.80$, $\varepsilon_{Hf}(500) = +25.7$) as well as radiogenic initial Sr isotopes ($I_{Sr} = 0.710$ vs $I_{Sr} = 0.709$–0.718 at 500 Ma for pyroxenites, Xiong et al., 2014). The gabbronorite also has arc-like enriched LREEs and Nb-Ta-Ti anomalies, indicating an origin of metasomatized lithospheric mantle. This interpretation is highly plausible although the exact mechanism is yet to be constrained with more data available in the future. Nevertheless, studies of the NQOB tectonic evolution history show that subduction of the Qilian Ocean began at ~520 Ma and completed at ~445 Ma (Song et al., 2013). Significant amount of the slab must have subducted to great depths to provide the needed water to weaken the SCLM and the ultimate emplacement of the Kekeli batholith (500 Ma).

The gabbronorite is characterised by high TiO_2 (3.02 wt %). High concentration of TiO_2 in the more evolved melts is a natural consequence of basaltic magma evolution (Dick et al., 2000; Niu et al., 2002). When ilmenite and pyroxenes crystallized from an evolved magma of SCLM origin at >1000 °C, they carry the SCLM isotopic composition with decoupled Nd-Hf isotopes. After the Ti-rich minerals crystallized, the remaining magma mixed with a granitic magma that carries the enriched un-decoupled Nd-Hf isotopes. This granitic magma could be derived from lower crust due to the underplating of the above-mentioned basaltic magma. With mixing/homogenising proceeding, the hybrid magmas progressively reached intermediate/andesitic composition and crystallized diorites with intermediate isotopic compositions. Compared to the intermediate hybrid magma from which the zircon crystallized, amphibole and plagioclase crystallized from a more mafic hybrid due to the relatively insufficient mixing thus carry the isotope signature closer to the mafic component or overlap those of host diorites, subsequently producing the discrepancy in Hf isotopes between zircon and bulk rock. As for the gabbronorite, ilmenite and pyroxene crystallized earlier from the parental basaltic magma, whereas zircon precipitated from a later hybrid granitic magma, thus having the largest Hf isotope discrepancy.

6.6. Implication

Zircon has been traditionally used to constrain the growth and differentiation of the continental crust due to its resistance, dating convenience and little radiogenic ^{176}Hf over time (because of relatively low Lu/Hf). Zircon Hf isotope analysis has become a powerful approach for understanding magmatic rocks (Patchett, 1983; Vervoort et al., 1996; Amelin et al., 2000; Kemp et al., 2007; Belousova et al., 2010; Iizuka et al., 2017). Indeed, Kemp et al. (2007) demonstrated that zircon Hf-O isotopes can be effectively used to trace the crust-mantle interaction. In the old orogenic belts where juvenile continent crust was possibly produced and preserved (Mo et al., 2008; Niu et al., 2013, Huang et al, 2014), the involvement of ancient lithologies is highly likely as evidenced by inherited zircon cores yet contribution of the mantle input requires quantitative modelling by means of isotopic mixing. Although zircon has been shown to have the advantage over the bulk rock compositions to unfold the timing and magnitude of mantle input in granitoids (Kemp et al., 2007) and most granites do not show discrepancy between zircon and whole rock Hf isotopes as observed in Kekeli Batholith, caution is necessary in using zircon alone as we show in this study.

Our study highlights the large discrepancy between zircon Hf isotopes and bulk rock Hf isotopes with the bulk rock having radiogenic Hf isotopes while zircons mostly have unradiogenic Hf isotopes. Although we did not analyse the Hf isotopes of Ti-minerals directly, it is likely that Ti-minerals have radiogenic Hf isotopes that caused the discrepancy between zircon and bulk rocks. During the open system process, mantle contribution to igneous rocks is thus substantially larger than recorded by zircons. Therefore, mantle magmas contribute more significantly to continental growth. This information is more preserved in the bulk rock, which is likely due to Ti-minerals, as we proposed above. Meanwhile, these samples also have bulk rock ε_{Hf}(t) compositions that decouple from their bulk-rock ε_{Nd}(t) while zircon ε_{Hf}(t) compositions do not. Pronounced Nd-Hf isotopic decoupling as well as the nature and the magnitude of the juvenile mantle input could be overlooked or underestimated if only zircon Hf isotopes were considered, which could mislead our quantitative understanding of the mantle contribution (vs. recycled, re-worked, old crustal materials) and hence the models of continental crustal growth. Thus, zircon Hf in such mixed magmas should not be used to define the evolution of mantle reservoirs. Therefore, cautions are needed before using zircon Hf isotopes to discuss the petrogenesis of igneous rocks that zircons do not always capture the full magmatic history of igneous rocks. By saying this, we do not oppose zircon to Ti-minerals but propose integrating zircon Hf isotopes with Hf information from Ti-minerals. This would help better

understand the petrogenesis and evolution of magmatic process that evolved in an open system involving interaction between isotopically-contrasting materials (different sources and/or different degrees of crustal contamination).

7. CONCLUSION

We present a range of new geochemical and isotope data for a sample suite from the Kekeli Batholith in the North Qilian Orogenic belt, Northern Tibetan plateau. Substantial discrepancy exists in the Hf isotope composition between bulk rocks and their constituent zircons. Bulk rock Nd-Hf isotopes exhibit pronounced decoupling whereas zircon Hf isotopes couple with bulk rock Nd isotopes. It is highly likely that early-formed Ti-rich minerals have different isotope signatures than those of later crystallized zircons from the same evolving and complex open magmatic systems. The following step to test this model is to analyse Hf isotopes of Ti-rich minerals directly. Our current findings propose that mantle input to igneous rocks formed by open system process is significantly larger than recorded by zircon and in such a case zircon Hf isotopes should not be used to define the evolution of the mantle reservoirs. We must realize that not all zircons yield unambiguous results. A better approach, in our view, is to simultaneously present Hf isotopes of whole rock or Ti-rich minerals as well.

ACKNOWLEDGEMENT

Hui Huang thanks Xuehui Yu, Xiaohong Xia, Pengyuan Guo, Piao'er Fu and Shuo Ding for field assistance. Hui thanks Lei Wu for trace elements analysis, Li Su for zircon dating, Yueheng Yang and Liewen Xie for zircon Hf isotope analysis, and Stuart Jones and Stephan Stricker for point counting. We thank Martin Guitreau and an anonymous reviewer for comments and suggestions that have helped improve this paper significantly. Further thanks go to Editor Maud Boyet for his editorial effort and constructive comments. The research was supported by Chinese NSFC grant (41130314, 41503007, 41630968), and the International Postdoctoral Exchange Fellowship Program.

APPENDIX A. SUPPLEMENTARY MATERIAL

Supplementary data to this article can be found online at https://doi.org/10.1016/j.gca.2019.05.031.

REFERENCES

Amelin Y., Lee D.-C. and Halliday A. N. (2000) Early-middle Archaean crustal evolution deduced from Lu–Hf and U-Pb isotopic studies of single zircon grains. *Geochim. Cosmochim. Acta* **64**, 4205–4225.

Bea F., Montero P. and Ortega M. (2006) A LA–ICP–MS evaluation of Zr reservoirs in common crustal rocks: Implications for Zr and Hf geochemistry, and zircon-forming processes. *Can. Mineral.* **44**(3), 693–714.

Bedini R. M., Blichert-Toft J., Boyet M. and Albarede F. (2002) Lu–Hf isotope geochemistry of garnet–peridotite xenoliths from the Kaapvaal craton and the thermal regime of the lithosphere. *Geochim. Cosmochim. Acta* **66**(S1), A61.

Belousova E. A., Kostitsyn Y. A., Griffin W. L., Begg G. C., O'Reilly S. Y. and Pearson N. J. (2010) The growth of the continental crust: constraints from zircon Hf-isotope data. *Lithos* **119**, 457–466.

Black L. P., Kamo S. L., Allen C. M., Aleinikoff J. N., Davis D. W., Korsch R. J. and Foudoulis C. (2003) TEMORA 1: a new zircon standard for Phanerozoic U-Pb geochronology. *Chem. Geol.* **200**, 155–170.

Blichert-Toft J., Arndt N. T. and Gruau G. (2004) Hf isotopic measurements on Barberton komatiites: effects of incomplete sample dissolution and importance for primary and secondary magmatic signatures. *Chem. Geol.* **207**(3), 261–275.

Boehnke P., Watson E. B., Trail D., Harrison T. M. and Schmitt A. K. (2013) Zircon saturation re-revisited. *Chem. Geol.* **351**, 324–334.

Bogaerts M., Scaillet B. and Auwera J. V. (2006) Phase Equilibria of the Lyngdal Granodiorite (Norway): Implications for the Origin of Metaluminous Ferroan Granitoids. *J. Petrol.* **47**, 2405–2431.

Bouvier A., Vervoort J. D. and Patchett P. J. (2008) The Lu—Hf and Sm—Nd isotopic composition of CHUR: constraints from unequilibrated chondrites and implications for the bulk composition of terrestrial planets. *Earth and Planetary Science Letters* **273**(1–2), 48–57.

Chauvel C., Lewin E., Carpentier M., Arndt N. T. and Marini J.-C. (2008) Role of recycled oceanic basalt and sediment in generating the Hf–Nd mantle array. *Nat. Geosci.* **1**, 64–67.

Chen L.-H., Zeng G., Jiang S.-Y., Hofmann A. W., Xu X.-S. and Pan M.-B. (2009) Sources of Anfengshan basalts: subducted lower crust in the Sulu UHP belt, China. *Earth Planet. Sci. Lett.* **286**, 426–435.

Chen Y. X., Song S. G., Niu Y. L. and Wei C. J. (2014) Melting of continental crust during subduction initiation: a case study from the Chaidanuo peraluminous granite in the North Qilian suture zone. *Geochim. Cosmochim. Acta* **132**, 311–336.

Chen S., Niu Y., Li J., Sun W., Zhang Y., Hu Y. and Shao F. (2016) Syn-collisional adakitic granodiorites formed by fractional crystallization: Insights from their enclosed mafic magmatic enclaves (MMEs) in the Qumushan pluton, North Qilian Orogen at the northern margin of the Tibetan Plateau. *Lithos* **248**, 455–468.

Chen L. M., Teng F. Z., Song X. Y., Hu R. Z., Yu S. Y., Zhu D. and Kang J. (2018) Magnesium isotopic evidence for chemical disequilibrium among cumulus minerals in layered mafic intrusion. *Earth Planet. Sci. Lett.* **487**, 74–83.

Chu M.-F., Chung S.-L., O'Reilly S. Y., Pearson N. J., Wu F.-Y., Li X.-H., Liu D., Ji J., Chu C.-H. and Lee H.-Y. (2011) India's hidden inputs to Tibetan orogeny revealed by Hf isotopes of Transhimalayan zircons and host rocks. *Earth Planet. Sci. Lett.* **307**, 479–486.

Couzinié S., Laurent O., Moyen J. F., Zeh A., Bouilhol P. and Villaros A. (2016) Post-collisional magmatism: Crustal growth not identified by zircon Hf–O isotopes. *Earth Planet. Sci. Lett.* **456**, 182–195.

DeLong S. E. and Chatelain C. (1990) Trace-element constraints on accessory-phase saturation in evolved MORB magma. *Earth Planet. Sci. Lett.* **101**, 206–215.

Dick H. J. B., Natland J. H., Alt J. C., Bach W., Bideau D., Gee J. S., Haggas S., Hertogen J. G. H., Hirth G., Holm P. M., Ildefonse B., Iturrino G. J., John B. E., Kelley D. S., Kikawa E., Kingdon A., LeRoux P. J., Maeda J., Meyer P. S., Miller D. J., Naslund H. R., Niu Y.-L., Robinson P. T., Snow J., Stephen R. A., Trimby P. W., Worm H.-U. and Yoshinobu A. (2000) A long in situ section of the lower ocean crust: results of ODP Leg 176 drilling at the Southwest Indian Ridge. *Earth Planet. Sci. Lett.* **179**, 31–51.

Dickinson, Jr., J. E. and Hess P. C. (1982) Zircon saturation in lunar basalts and granites. *Earth Planet. Sci. Lett.* **57**(2), 336–344.

Dowall D. P., Nowell G. M. and Pearson D. G. (2003) *Chemical preconcentration procedures for high-precision analysis of Hf-Nd-Sr isotopes in geological materials by plasma ionisation multicollector mass spectrometry (PIMMS) techniques. Plasma Source Mass Spectrometry: Applications and Emerging Technologies*. Royal Society of Chemistry, Cambridge, pp. 321–337.

Elhlou S., Belousova E., Griffin W. L., Pearson N. J. and O'Reilly S. Y. (2006) Trace element and isotopic composition of GJ red zircon standard by laser ablation. *Geochim. Cosmochim. Acta* **70**, A158.

Farina F., Stevens G., Gerdes A. and Frei D. (2014) Small-scale Hf isotopic variability in the Peninsula pluton (South Africa): the processes that control inheritance of source 176 Hf/177 Hf diversity in S-type granites. *Contrib. Miner. Petrol.* **168**(4), 1065.

Ferry J. M. and Watson E. B. (2007) New thermodynamic models and revised calibrations for the Ti-in-zircon and Zr-in-rutile thermometers. *Contrib. Miner. Petrol.* **154**(4), 429–437.

Fisher C. M., Vervoort J. D. and Hanchar J. M. (2014) Guidelines for reporting zircon Hf isotopic data by LA–MC–ICPMS and potential pitfalls in the interpretation of these data. *Chem. Geol.* **363**, 125–133.

Galer S. J. (1999) Optimal double and triple spiking for high precision lead isotopic measurement. *Chem. Geol.* **157**(3), 255–274.

Gerdes A. and Zeh A. (2009) Zircon formation versus zircon alteration—new insights from combined U-Pb and Lu–Hf in-situ LA-ICP-MS analyses, and consequences for the interpretation of Archean zircon from the Central Zone of the Limpopo Belt. *Chem. Geol.* **261**(3–4), 230–243.

Gerdes, A. (2012). Apparent Crustal Growth due to Disequilibration of the Lu-Hf Isotope System during Crustal Melting. In Goldschmidt 2012 Conference Abstracts.

Green T. H. (1994) Experimental studies of trace-element partitioning applicable to igneous petrogenesis—Sedona 16 years later. *Chem. Geol.* **117**(1), 1–36.

Guitreau M., Blichert-Toft J., Martin H., Mojzsis S. J. and Albarède F. (2012) Hafnium isotope evidence from Archean granitic rocks for deep-mantle origin of continental crust. *Earth Planet. Sci. Lett.* **337**, 211–223.

Griffin W. L., Pearson N. J., Belousova E., Jackson S. E., van Achterbergh E., O'Reilly S. Y. and Shee S. R. (2000) The Hf isotope composition of cratonic mantle: LAM-MC-ICPMS analysis of zircon megacrysts in kimberlites. *Geochim. Cosmochim. Acta* **64**, 133–147.

Hanchar J. M. and Watson E. B. (2003) Zircon saturation thermometry. *Rev. Mineral. Geochem.*, 89–112.

Heinonen A. P., Andersen T. and Ramo O. T. (2010) Re-evaluation of Rapakivi Petrogenesis: Source Constraints from the Hf Isotope Composition of Zircon in the Rapakivi Granites and Associated Mafic Rocks of Southern Finland. *J. Petrol.* **51**, 1687–1709.

Hoffmann J. E., Münker C., Polat A., König S., Mezger K. and Rosing M. T. (2010) Highly depleted Hadean mantle reservoirs in the sources of early Archean arc-like rocks, Isua supracrustal belt, southern West Greenland. *Geochim. Cosmochim. Acta* **74** (24), 7236–7260.

Hoskin P. W. (2005) Trace-element composition of hydrothermal zircon and the alteration of Hadean zircon from the Jack Hills, Australia. *Geochim. Cosmochim. Acta* **69**(3), 637–648.

Hoskin P. W. and Schaltegger U. (2003) The composition of zircon and igneous and metamorphic petrogenesis. *Rev. Mineral. Geochem.* **53**(1), 27–62.

Hilyard M., Nielsen R. L., Beard J. S., Patinō-Douce A. and Blencoe J. (2000) Experimental determination of the partitioning behavior of rare earth and high field strength elements between pargasitic amphibole and natural silicate melts. *Geochim. Cosmochim. Acta* **64**, 1103–1120.

Huang H., Niu Y., Nowell G., Zhao Z., Yu X., Zhu D. C., Mo X. and Ding S. (2014) Geochemical constraints on the petrogenesis of granitoids in the East Kunlun Orogenic belt, northern Tibetan Plateau: Implications for continental crust growth through syn-collisional felsic magmatism. *Chem. Geol.* **370**, 1–18.

Huang H., Niu Y. and Mo X. (2017) Garnet effect on Nd-Hf isotope decoupling: evidence from the Jinfosi batholith, Northern Tibetan Plateau. *Lithos* **274**, 31–38.

Iizuka T., Yamaguchi T. and Itano K., et al. (2017) What Hf isotopes in zircon tell us about crust–mantle evolution. *Lithos* **274–275**, 304–327.

Jackson S. E., Pearson N. J., Griffin W. L. and Belousova E. A. (2003) The application of laser ablation-inductively coupled plasma-mass spectrometry to in situ U-Pb zircon geochronology. *Chem. Geol.* **211**, 47–69.

Jang Y. D. and Naslund H. R. (2003) Major and trace element variation in ilmenite in the Skaergaard Intrusion: petrologic implications. *Chem. Geol.* **193**(1–2), 109–125.

Jaffey A. H., Flynn K. F., Glendenin L. E., Bentley W. T. and Essling A. M. (1971) Precision measurement of half-lives and specific activities of U 235 and U 238. *Physical Review C* **4**(5), 1889.

Kemp A. et al. (2007) Magmatic and crustal differentiation history of granitic rocks from Hf-O isotopes in zircon. *Science* **315** (5814), 980.

Kirkland C. L., Smithies R. H., Taylor R. J. M., Evans N. and Mcdonald B. (2015) Zircon Th/U ratios in magmatic environs. *Lithos* **212–215**, 397–414.

Li X.-H., Li W.-X., Li Q.-L., Wang X.-C., Liu Y. and Yang Y.-H. (2010) Petrogenesis and tectonic significance of the ~850 Ma Gangbian alkaline complex in South China: Evidence from in situ zircon U-Pb dating, Hf–O isotopes and whole-rock geochemistry. *Lithos* **114**, 1–15.

Li X. L., Chen X., Ge H. J., Wu Y. T., Xian X. L. and Han W. (2011) XRF determination of chlorine etc multi-elements in sea sediments with sample preparation by fusion. *Phys. Test. Chem. Anal. B Chem. Anal.* **47**, 1420–1423 (in Chinese with English abstract).

Liu Y. J., Neubauer F., Genser J., Takasu A., Ge X.-H. and Handler R. (2006) 40Ar/39Ar ages of blueschist facies pelitic schists from Qingshuigou in the Northern Qilian Mountains, western China. *Isl. Arc* **15**, 187–198.

Liu Y. S., Hu Z. C., Gao S., Gunther D., Xu J., Gao C. G. and Chen H. H. (2008a) In situ analysis of major and trace elements of anhydrous minerals by LA-ICP-MS without applying an internal standard. *Chem. Geol.* **257**, 34–43.

Liu Y. S., Hu Z. C., Gao S., Gunther D., Xu J., Gao C. G. and Chen H. H. (2008b) In situ analysis of major and trace elements of anhydrous minerals by LA-ICP-MS without applying an internal standard. *Chem. Geol.* **257**(1–2), 34–43.

Liu S. A., Teng F. Z., He Y., Ke S. and Li S. (2010) Investigation of magnesium isotope fractionation during granite differentiation: implication for Mg isotopic composition of the continental crust. *Earth Planet. Sci. Lett.* **297**(3–4), 646–654.

Lin Y. H., Zhang L. F., Ji J. Q. and Song S. G. (2010) 40Ar/39Ar age of Jiugequan lawsoniteblueschists in northern Qilian Mountains and its petrologic significance. *Chin. Sci. Bull.* **55**, 2021–2027.

Ludwig K. R. (2003) A Geochronological Toolkit for Microsoft Excel. *Isoplot* **3**, 1–70.

Lugmair G. W. and Marti K. (1978) Lunar initial 143Nd/144Nd: differential evolution of the lunar crust and mantle. *Earth and Planetary Science Letters* **39**(3), 349–357.

Miller C. F., McDowell S. M. and Mapes R. W. (2003) Hot and cold granites? Implications of zircon saturation temperatures and preservation of inheritance. *Geology* **31**(6), 529–532.

Mo X. X., Niu Y. L., Dong G. C., Zhao Z. D., Hou Z. Q., Zhou S. and Ke S. (2008) Contribution of syncollisional felsic magmatism to continental crust growth: a case study of the Paleogene Linzizong volcanic succession in southern Tibet. *Chem. Geol.* **250**, 49–67.

Nash W. and Crecraft H. (1985) Partition coefficients for trace elements in silicic magmas. *Geochim. Cosmochim. Acta* **49**, 2309–2322.

Niu Y. L. (2005) Generation and evolution of basaltic magmas: some basic concepts and a new view on the origin of Mesozoic-Cenozoic basaltic volcanism in eastern China. *Geol. J. China Univ.* **11**(1), 9–46.

Niu Y. L. (2014) Geological understanding of plate tectonics: Basic concepts, illustrations, examples and new perspectives. *Global Tecton. Metall.* **10**, 23–46.

Niu, Y., Gilmore, T., Mackie, S., Greig, A., and Bach, W. (2002). Mineral chemistry, whole-rock compositions, and petrogenesis of Leg 176 gabbros: data and discussion. In Proceedings of the Ocean Drilling Program, Scientific Results.pp.1–60.

Niu Y., Zhao Z., Zhu D. C. and Mo X. (2013) Continental collision zones are primary sites for net continental crust growth—a testable hypothesis. *Earth Sci. Rev.* **127**, 96–110.

Nowell G. M., Kempton P. D., Noble S. R., Fitton J. G., Sauders A. D., Mahoney J. J. and Taylor R. N. (1998) High precision Hf isotope measurements of MORB and OIB by thermal ionisation mass spectrometry: insights into the depleted mantle. *Chem. Geol.* **149**, 211–233.

Nowell G. M., Pearson D. G., Ottley C. J., Schweiters J. and Dowall D. (2003) *Long-term performance characteristics of a plasma ionisation multi-collector mass spectrometer (PIMMS): the thermofinnigan neptune*. Applications and Emerging Technologies Royal Society of Chemistry, Cambridge, Plasma Source Mass Spectrometry, pp. 307–320.

Nowell G. M., Pearson D. G., Bell D. R., Carlson R. W., Smith C. B., Kempton P. D. and Noble S. R. (2004) Hf Isotope Systematics of Kimberlites and their Megacrysts: New Constraints on their Source Regions. *J. Petrol.* **45**, 1583–1612.

Onuma N., Higuchi H., Wakita H. and Nagasawa H. (1968) Trace element partition between two pyroxenes and the host lava. *Earth Planet. Sci. Lett.* **5**, 47–51.

Patchett P. J. (1983) Importance of the Lu-Hf isotopic system in studies of planetary chronology and chemical evolution. *Geochim. Cosmochim. Acta* **47**, 81–91.

Pankhurst M. J., Schaefer B. F., Turner S. P., Argles T. and Wade C. E. (2013) The source of A-type magmas in two contrasting settings: U-Pb, Lu–Hf and Re–Os isotopic constraints. *Chem. Geol.* **351**, 175–194.

Pearce N. J. G. (1990) Zirconium and niobium-bearing ilmenites from the Igaliko dyke swarm, South Greenland. *Mineral. Mag.* **54**(377), 585–588.

Pearson, D., and Nowell, G. (2003). Dating Mantle Differentiation: a comparison of the Lu-Hf, Re-Os &Sm-Nd isotope systems in the Beni Bousera peridotite massif and constraints on the Nd-Hf isotope composition of the lithospheric mantle, EGS-AGU-EUG Joint Assembly, p. 5430.

Rizo H., Boyet M., Blichert-Toft J. and Rosing M. (2011) Combined Nd and Hf isotope evidence for deep-seated source of Isua lavas. *Earth Planet. Sci. Lett.* **312**(3–4), 267–279.

Salters V. J. M. and Zindler A. (1995) Extreme 176Hf/177Hf in the sub-oceanic mantle. *Earth Planet. Sci. Lett.* **129**, 13–30.

Schmidberger S. S., Simonetti A. and Francis D. (2002) Probing Archean lithosphere using the Lu–Hf systematics of peridotite xenoliths from Somerset Island kimberlites, Canada. *Earth Planet. Sci. Lett.* **197**, 245–259.

Schmitz M. D., Vervoort J. D., Bowring S. A. and Patchett P. J. (2004) Decoupling of the Lu-Hf and Sm-Nd isotope systems during the evolution of granulitic lower crust beneath southern Africa. *Geology* **32**, 405.

Shi R. D., Yang J., Wu C. l., IIzuka T. and Hirata T. (2004) Island Arc volcanic rocks in North Qaidam UHP metamorphic belt. *Acta Geol. Sin.* **78**(52), 64 (in Chinese with English abstract).

Simon N. S. C., Carlson R. W., Pearson D. G. and Davies G. R. (2002) The Lu–Hf isotope composition of cratonic lithosphere: disequilibrium between garnet and clinopyroxene in kimberlite xenoliths. *Geochim. Cosmochim. Acta* **66**(S1), A717.

Simon N. S. C., Irvine G. J., Davies G. R., Pearson D. G. and Carlson R. W. (2003) The origin of garnet and clinopyroxene in 'depleted' Kaapvaal peridotites. *Lithos* **71**, 289–322.

Söderlund U., Patchett P. J., Vervoort J. D. and Isachsen C. E. (2004) The 176Lu decay constant determined by Lu–Hf and U–Pb isotope systematics of Precambrian mafic intrusions. *Earth and Planetary Science Letters* **219**(3–4), 311–324.

Song S., Zhang L., Niu Y., Song B., Zhang G. and Wang Q. (2004) Zircon U-Pb SHRIMP ages of eclogites from the North Qilian Mountains in NW China and their tectonic implication. *Chin. Sci. Bull.* **49**, 848–852.

Song S., Zhang L., Niu Y., Su L., Song B. and Liu D. (2006) Evolution from oceanic subduction to continental collision: a case study from the Northern Tibetan Plateau based on geochemical and geochronological data. *J. Petrol.* **47**(3), 435–455.

Song S. G., Zhang L. F., Niu Y. L., Wei C. J., Liou J. G. and Shu G. M. (2007) Eclogite and carpholite-bearing meta-pelite in the North Qilian suture zone, NW China: implications for Paleozoic cold oceanic subduction and water transport into mantle. *J. Metamorph. Geol.* **25**, 547–563.

Song S., Niu Y. L., Zhang L. F. and Zhang G. B. (2009) Time constraints on orogenesis from oceanic subduction to continental subduction, collision, and exhumation: an example from North Qilian and North Qaidam HP–UHP belts. *Acta Petrol. Sinica* **25**, 2067–2077.

Song S., Niu Y. L., Wei C. J., Ji J. Q. and Su L. (2010) Metamorphism, anatexis, zircon ages and tectonic evolution of the Gongshan Block in the northern Indochina continent—an eastern extension of Lhasa Block. *Lithos* **120**, 3–4.

Song S., Niu Y., Su L. and Xia X. (2013) Tectonics of the North Qilian orogen, NW China. *Gondwana Res.* **23**, 1378–1401.

Steiger R. and Jäger E. (1977) Subcommission on geochronology: convention on the use of decay constants in geo-and cosmochronology. *Earth and planetary science letters* **36**(3), 359–362.

Sun S.-S. and McDonough W. F. (1989) Chemical and isotopic systematics of oceanic basalts: implications for mantle composition and processes. *Geological Society, London, Special Publications* **42**, 313–345.

Tappe S., Foley S. F., Stracke A., Romer R. L., Kjarsgaard B. A., Heaman L. M. and Joyce N. (2007) Craton reactivation on the Labrador Sea margins: 40Ar/39Ar age and Sr-Nd-Hf-Pb isotope constraints from alkaline and carbonatite intrusives. *Earth Planet. Sci. Lett.* **256**(3), 433–454.

Tappe S., Foley S. F., Kjarsgaard B. A., Romer R. L., Heaman L. M. and Stracke A., et al. (2008) Between carbonatite and lamproite—diamondiferous torngat ultramafic lamprophyres formed by carbonate-fluxed melting of cratonic marid-type metasomes. *Geochim. Cosmochim. Acta* **72**(13).

Tang M., Wang X. L., Shu X. J., Wang D., Yang T. and Gopon P. (2014) Hafnium isotopic heterogeneity in zircons from granitic rocks: Geochemical evaluation and modeling of "zircon effect" in crustal anatexis. *Earth Planet. Sci. Lett.* **389**, 188–199.

Teng F. Z., Li W. Y., Ke S., Yang W., Liu S. A., Sedaghatpour F., Wang S. J., Huang K. J., Hu Y., Ling M. X. and Xiao Y. (2015) Magnesium isotopic compositions of international geological reference materials. *Geostand. Geoanal. Res.* **39**(3), 329–339.

Thirlwall M. F. (1991) Long-term reproducibility of multi-collector Sr and Nd isotope ratio analysis. *Chem. Geol.: Isotope Geosci. Section* **94**, 85–104.

Tseng C. Y., Yang H. J., Yang H. Y., Liu D., Tsai C. L., Wu H. and Zuo G. (2007) The Dongcaohe ophiolite from the North Qilian Mountains: a fossil oceanic crust of the Paleo-Qilian ocean. *Chin. Sci. Bull.* **52**(17), 2390–2401.

Vervoort J. D., Patchett P. J., Gehrels G. E. and Nutman A. P. (1996) Constraints on early Earth differentiation from Hf isotopes. *Nature* **379**, 624–627.

Vervoort J. D. and Blichert-Toft J. (1999) Evolution of the depleted mantle: Hf isotope evidence from juvenile rocks through time. *Geochim. Cosmochim. Acta* **63**, 533–556.

Wang C. Y., Zhang Q., Qian Q. and Zhou M. F. (2005) Geochemistry of the Early Paleozoic Baiyin volcanic rocks (NW China): implications for the tectonic evolution of the North Qilian orogenic belt. *J. Geol.* **113**(1), 83–94.

Wang S. J., Teng F. Z., Li S. G. and Hong J. A. (2014) Magnesium isotopic systematics of mafic rocks during continental subduction. *Geochim. Cosmochim. Acta* **143**, 34–48.

Wang D., Wang X. L., Cai Y., Goldstein S. L. and Yang T. (2017) Do Hf isotopes in magmatic zircons represent those of their host rocks? *J. Asian Earth Sci.*. https://doi.org/10.1016/j.jseaes.2017.12.025.

Weis D., Kieffer B., Maerschalk C., Pretorius W. and Barling J. (2005) High-precision Pb-Sr-Nd-Hf isotopic characterization of USGS BHVO-1 and BHVO-2 reference materials. *Geochem. Geophys. Geosyst.* **6**(2).

Weis D., Kieffer B., Hanano D., Nobre Silva I., Barling J., Pretorius W. and Mattielli N. (2007) Hf isotope compositions of US Geological Survey reference materials. *Geochem. Geophys. Geosyst.* **8**(6).

Wiedenbeck M., Alle P., Corfu F., Griffin W., Meier M., Oberli F., Quadt A. v., Roddick J. and Spiegel W. (1995) Three natural zircon standards for U-Th-Pb, Lu-Hf, trace element and REE analyses. *Geostandards Newslett.* **19**, 1–23.

Wood B. J. and Blundy J. D. (1997) A predictive model for rare earth element partitioning between clinopyroxene and anhydrous silicate melt. *Contrib. Miner. Petrol.* **129**, 166–181.

Woodhead J. D. and Hergt J. M. (2005) A preliminary appraisal of seven natural zircon reference materials for in situ hf isotope determination. *Geostand. Geoanal. Res.* **29**(2), 183–195.

Wu C. L., Xu X. Y., Gao Q. M., Li X. M. and Lei M., et al. (2010) Early Palaezoic granitoid magmatism and tectonic evolution in North Qilian, NW China. *Acta Petrol. Sinica* **26**, 1027–1044 (in Chinese with English abstract).

Wu H. Q., Feng Y. M. and Song S. G. (1993) Metamorphism and deformation of blueschist belts and their tectonic implications, North Qilian Mountains, China. *J. Metamorph. Geol.* **11**, 523–536.

Wu F.-Y., Yang Y.-H., Xie L.-W., Yang J.-H. and Xu P. (2006) Hf isotopic compositions of the standard zircons and baddeleyites used in U-Pb geochronology. *Chem. Geol.* **234**, 105–126.

Xia X. and Song S. (2010) Forming age and tectono-petrogenises of the Jiugequan ophiolite in the North Qilian Mountain, NW China. *Chin. Sci. Bull.* **55**, 1899–1907.

Xia X., Song S. and Niu Y. (2012) Tholeiite–boninite terrane in the North Qilian suture zone: Implications for subduction initiation and back-arc basin development. *Chem. Geol.* **328**, 259–277.

Xiong Q., Zheng J. P., Griffin W. L., O'reilly S. Y. and Pearson N. J. (2014) Pyroxenite dykes in orogenic peridotite from North Qaidam (NE Tibet, China) track metasomatism and segregation in the mantle wedge. *J. Petrol.* **55**(12), 2347–2376.

Xiong Q., Griffin W. L., Zheng J. P., O'Reilly S. Y. and Pearson N. J. (2015) Episodic refertilization and metasomatism of Archean mantle: evidence from an orogenic peridotite in North Qaidam (NE Tibet, China). *Contrib. Miner. Petrol.* **169**(3), 31.

Yu X. N., Song S. G., Wei C. J. and Zhang L. F. (2009) Mg-carpholite metapelite and its implications for ancient oceanic subduction in the North Qilian suture zone, NW China. *Acta Scientiarum Naturalium Universitatis Pekinensis* **45**, 472–480.

Yuan H. L., Gao S., Dai M. L., Zong C. L., Gunther D., Fontaine G. H., Liu X. M. and Diwu C. R. (2008) Simultaneous determinations of U-Pb age, Hf isotopes and trace element compositions of zircon by excimer laser-ablation quadrupole and multiple-collector ICPMS. *Chem. Geol.* **247**(1), 100–118.

Zeng G., Chen L.-H., Hofmann A. W., Jiang S.-Y. and Xu X.-S. (2011) Crust recycling in the sources of two parallel volcanic chains in Shandong, North China. *Earth Planet. Sci. Lett.* **302**, 359–368.

Zheng Y. F., Zhao Z. F., Wu Y. B., Zhang S. B., Liu X. and Wu F. Y. (2006) Zircon U-Pb age, Hf and O isotope constraints on protolith origin of ultrahigh-pressure eclogite and gneiss in the Dabie orogen. *Chem. Geol.* **231**(1–2), 135–158.

Zhang J., Xu Z., Chen W. and Xu H. (1997) A tentative discussion on the ages of the subduction–accretionary complex/volcanic arcs in the middle sector of North Qilian Mountain. *Acta Petrol. Mineral.* **16**, 112–119.

Zhang J. X., Meng F. C. and Wan Y. S. (2007) A cold Early Palaeozoic subduction zone in the North Qilian Mountains, NW China: petrological and U-Pb geochronological constraints. *J. Metamorph. Geol.* **25**, 285–304.

Zhang L., Wang Q. and Song S. (2009) Lawsonite blueschist in Northern Qilian, NW China: P-T pseudosections and petrologic implications. *J. Asian Earth Sci.* **35**(3), 354–366.

Associate editor: Maud Boyet